

TU DELFT, FACULTY OF ELECTRICAL ENGINEERING,
MATHEMATICS AND COMPUTER SCIENCE FACULTY OF
APPLIED SCIENCES

BACHELOR THESIS OF
BSc PROGRAM APPLIED MATHEMATICS AND BSc PROGRAM APPLIED PHYSICS

Two-dimensional morphodynamical equilibria in a double inlet system

Author:

Billy Verhage,
Student number: 4717074

Supervisors:

Prof. Dr. H. M. Schuttelaars
Dr. S. R. de Roode



April 30, 2021

Abstract

In this thesis, the foundations are explored for establishing two-dimensional depth-integrated morphodynamical equilibria for a long embayment with two tidal inlets connected to the open sea. Governing water motion, suspended sediment transport and bed evolution equations had to be re-derived from the underlying balances, where the tidal inlets are prescribed by M_2 forcing, and the bedload transport is primarily due to the slope gradient. The equilibrium solutions are determined by an asymptotic expansion in a small parameter and applying a temporal Fourier series up to the leading order term. From this, a solvable system of six partial differential equations is derived. Using finite-difference discretization, this system of partial differential equations is turned into a discrete lexicographically ordered system of nonlinear constraints. The Newton-Rapsons method is used in a newly developed code to be able to produce morphodynamical equilibrium solutions. When the cross-sectional discretization contains only one interior point, the solutions are in accordance with the cross-sectional model. In particular, the more complex bifurcation structure arises after variation of the tidal phase, amplitude and inlet depth. This strengthens the recent findings of complex bifurcation structures. These width-averaged equilibria seem to stay accurate equilibria in the cross-sectional expanded model even for the more complex behaviour. The question of these equilibria are stable cannot be answered as firmly as some unexplained behaviour arose during the analysis of the eigenvalues. However, these results hint that the width-averaged equilibria remain stable until the width of the channel is half its length. Further research is needed to prove this.

Preface

You are about to read my thesis, in which I explored the mathematics and physics behind complex morphodynamical systems. My name is Billy, and I am a fourth year double bachelor student. This thesis has been written to fulfil my double bachelor's degree, Applied Physics and Applied Mathematics at the Delft University of Technology. I worked on this thesis simultaneously with my last few courses from November 2020 until April 2021. The underlying complexity of these seemingly simple systems still amazes me, and I hope that after reading this some of my excitement passes over. Although Albert Einstein was not amused that his mentor Hendrik Antoon Lorentz spent his last few years laying the foundations of the morphodynamical theory used today, I am very grateful he did.

This thesis would not be possible without the help and support of others, so I would like to make my acknowledgements. First and foremost, I would like to thank Prof. Dr H. M. Schuttelaars and Dr. S. R. de Roode for the great supervision and guidance I received during this thesis. I am especially grateful to Prof. Dr. H. M. Schuttelaars for the time he took for finding my grammatical errors. Furthermore, I would like to thank my assessment committee for taking their time to analyse my thesis. Additionally, I would like to thank my friends Ian Luik, Jan Bosma, Jort Bouma, Jort de Groot, José Dupont, Rona Roovers, Sarah Jansen and Storm Diephuis for keeping me sharp and motivated during my studies. Finally, I would like to thank my parents for their unconditional love and support.

I hope you enjoy your reading.

Billy Verhage

Table of contents

1	Introduction	1
2	Depth-averaged morphodynamic model	3
2.1	Geometry of the domain	3
2.2	Depth-averaged shallow water equations	3
2.3	Suspended sediment transport, erosion and sedimentation	4
2.4	Bed evolution	5
3	Solving the model	7
3.1	Scaling the system of equations	7
3.2	Expansion in tidal components	8
3.2.1	Solving the shallow water equation in tidal components	8
3.2.2	Solving the sediment concentration in tidal components	10
3.2.3	Solving the equilibrium bathymetry	11
3.2.4	System of partial differential equations	12
4	Numerical method	13
4.1	Newton-Raphson method	13
4.2	Restating as an implicit function	13
4.3	Discretization	14
4.4	Jacobian	14
4.5	Stability analysis	15
5	Results and Discussion	16
5.1	Parameter values of the Marsdiep Vlie system	16
5.2	Typical solution analysis	17
5.3	Variation of parameters.	20
5.3.1	Variation of tidal phase difference experiment.	20
5.3.2	Variation of incoming wave amplitude.	21
5.3.3	Variation of inlet depth.	22
5.4	Stability of the width-averaged equilibrium solutions in two dimensions.	23
5.5	Two-dimensional variation of channel width.	25
6	Conclusion	26
	Bibliography	27
	Appendix	28
A	Derivation of depth-averaged shallow water equations	29
A.1	Three-dimensional Reynolds averaged water equations	29
A.2	Depth-averaged conservation of mass	31
A.3	Depth-averaged conservation of momentum	31
B	Derivation of suspended sediment concentration equation	35
C	The boundary conditions of the discretization	38

1 Introduction

Currently, global warming is one of the most pressing topics on the international agenda. Most governments have recognized its dangerous consequences and see the importance of preventing the average global temperature from rising by more than 2 degrees Celsius. However, even if this goal is reached, the IPCC still predicts that the sea level will rise 0.3 to 0.6 meter by 2100, as stated in Oppenheimer et al. (2019). Consequently, once in a century storms would become annual by 2050. This would significantly increase the risk of flooding of low-lying densely populated areas.

The Netherlands has a long history fighting the sea. In the past, it has faced large floods with many casualties. For example, the North Sea flood of 1953. As a response to these floods, most natural estuaries were disconnected from the sea by large projects like the Delta works or further back in time (1929) the enclosure dam called the "Afsluitdijk" (see figure 1). These projects greatly decreased the risk of flooding in the Netherlands.



Figure 1: The Marsdiep inlet (denoted by I) to the Vlie inlet (denoted by II) system in the Wadden sea. The enclosure dam 'Afsluitdijk' in the bottom right corner disconnects the IJsselmeer and the Wadden Sea. Satellite image from zoom earth (n.d.)

However, during their construction, the long time morphodynamical consequences were not yet considered. The construction of the enclosure dam resulted in a morphological imbalance in the Wadden Sea. Recent studies show that the Wadden Sea is still changing to a new equilibrium. (Elias et al. (2012).) As a consequence morphological changes such as erosion of coastlines and changing channel-shoal patterns still occur. Not only human intervention will result in morphological adaptations, climate change will also affect morphology.

As rising sea level due to climate change is a fact, a large number of the sea connected channels around the world might become morphologically unstable and face devastating morphological consequences like floods. To properly anticipate the long-term effects, morphodynamical models can be used, see for example de Swart and Schuttelaars (1997) or de Swart and Zimmerman (2009). These models simulate the morphological evolution of channels that have a single connection to the open sea are called single inlets systems. Double inlet systems such as those observed in the Wadden Sea were not considered. To get insight in their morphological behaviour, the model developed in de Swart and Schuttelaars (1997) was extended by Deng et al. (2020) to determine and explore the morphodynamical equilibria of double inlet systems

The articles above use cross-sectionally averaged one-dimensional morphodynamical models. During this thesis, I explored the validity of this assumption by deriving a two-dimensional depth-averaged morphodynamical model for a double inlet system. The following research questions will be considered:

- **RQ1:** What is the linear stability of the one-dimensional morphodynamical equilibria of double inlet systems under the variation of inlet parameters?
- **RQ2:** How stable are these solutions for two-dimensional perturbations and, how does the stability change under variation of channel width?

I analyse the stability of one-dimensional equilibria in the extended two-dimensional model using a newly developed code. The results obtained with the model were interpreted in terms of physical mechanisms. Although the model is general, the results are obtained using parameter values representative of the Marsdiep Vlie system, a double inlet system in the Dutch Wadden Sea, shown in figure 1.

This thesis consists of six chapters and one appendix. In chapter 2 the conservation equations governing the morphodynamical evolution are given. The derivation of these equations from the three-dimensional balances are treated in Appendixes A and B. Chapter 3 describes the method used to obtain the equilibrium solution. In chapter 4 the numerical implementation is described and analysed. The results are studied and discussed in chapter 5, followed by the conclusion in chapter 6.

2 Depth-averaged morphodynamic model

Using a morphodynamic model the changes of the bed over time can be obtained. Since the change in the bed topology results in changes in the flow of water and sediment transport, such changes in turn result in changes of the bed. Consequently, a morphodynamical model calculates the water movement, sediment concentration and bed evolution simultaneously.

The geometry of the domain under consideration is discussed. Next, the depth-averaged shallow water equations and the associated boundary conditions are introduced, followed by the suspended sediment equation. Finally, the associated bed evolution is introduced.

2.1 Geometry of the domain

The domain under consideration has a rectangular geometry with length L and width B , with $L \approx 60\text{km}$ and $B \approx 1\text{km}$. The double inlet system is discussed in detail in chapter five. A top view and side view are shown in figure 2. Both the left and right sides of the channel are connected to the open sea. The left inlet at $x = 0$, called inlet I , has a undisturbed water depth of H^I . The right inlet located at $x = L$ and called inlet II has an undisturbed water depth of H^{II} . The South ($y = 0$) and North ($y = B$) boundaries are assumed to be vertical walls, impenetrable to water and sediment. The water depth is defined as $H^I - h + \zeta$, where ζ is the surface water level and h , is the denotes the height of the bed profiled measured from H^I .

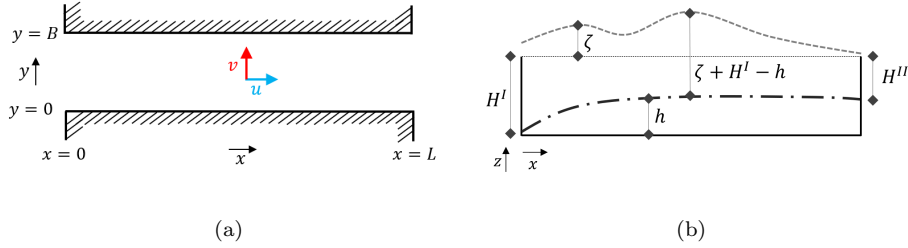


Figure 2:

- (a) Top view of the rectangular domain. Left and right boundaries are connected to the open sea. The North and South boundaries are closed. The horizontal water motion is denoted by u and the vertical water motion is denoted by v .
- (b) A side view of the model. In this figure, ζ denotes the water surface height measured from a fixed undisturbed water level, h denotes the height of the bed profiles measured from H^I .

2.2 Depth-averaged shallow water equations

The physical variables describing the water motion are:

- $\zeta(t, x, y)$, the height of a water column with respect to the undisturbed water depth at any given location.
- $\mathbf{u}(t, x, y) = [u(t, x, y), v(t, x, y)]^T$, the depth-averaged water velocity, in the x and y direction, respectively.

The bathymetry $h(t, x, y)$ is assumed to be known for now. The dynamical behaviour of the quantities follows from the conservation of mass and impulse. The water motion is forced by a tidal signal at both open boundaries. For the system under consideration the conservation laws are given by the depth-averaged shallow water equations:

$$\nabla_{xy} \cdot ((H^I + \zeta - h)\mathbf{u}) = -\zeta_t + h_t, \quad (2.1)$$

$$\mathbf{u}_t + [\mathbf{u} \cdot \nabla_{xy}]\mathbf{u} = -g\nabla_{xy}\zeta + \frac{-r}{H^I + \zeta - h}\mathbf{u}, \quad (2.2)$$

where $\nabla_{xy} \equiv [\frac{\partial}{\partial x}, \frac{\partial}{\partial y}]^T$ denotes the two-dimensional differential operator, time is defined by t , g denotes the acceleration by gravity and r the bed friction coefficient. The first term of Eq. (2.1) is the divergence of the water in a column that is connected to the temporal change in the height of the water column by the second and third terms. The first term of Eq. (2.2) is the local inertia, the second term captures convection, the third term the pressure gradient and the final term the bed friction. For details about the derivation of the depth averaged equations from the three-dimensional balances, see Appendix A.

Boundary conditions

The water motion is forced by prescribed free surface elevation at $x = 0$ and $x = L$. These surface elevations are related to the tides in the open sea. Focusing on the main tidal constituent, the boundaries read:

$$\begin{aligned} \zeta(t, x, y) &= A^I \cos(\sigma t - \phi^I), & x = 0, \\ \zeta(t, x, y) &= A^{II} \cos(\sigma t - \phi^{II}), & x = L, \end{aligned} \quad (2.3)$$

where the radial frequency σ is $2\pi/T_{tide}$ where $T_{tide} = 12h25m = 44.9 \cdot 10^3 s$. The amplitudes of the forcing at the respective inlets are A^I and A^{II} , and the tidal phases are given by ϕ^I and ϕ^{II} . The north and the south boundaries are closed, requiring no water transport through their boundaries:

$$\begin{aligned} [(H^I + \zeta - h)\mathbf{u}] \cdot \hat{\mathbf{y}} &= 0, & y = 0, \\ [(H^{II} + \zeta - h)\mathbf{u}] \cdot \hat{\mathbf{y}} &= 0, & y = B. \end{aligned} \quad (2.4)$$

2.3 Suspended sediment transport, erosion and sedimentation

The shear stresses exerted by the bottom on the water motion slow down the flow. In turn, these stresses exerted by the fluid on the bottom result in erosion of the bed material. The sediment particles are lifted in the water column and can be transported by diffusive and convective processes. Finally, the suspended sediment can settle on the bed under the influence of gravity. A graphical representation is given in figure 3.

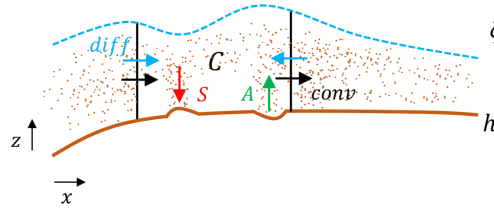


Figure 3: Side view of suspended sediment transport. Here \mathcal{C} is the depth-integrated concentration of sediment particles (dots) in an infinitesimally small water column. Settling of sediment is characterized by S . The erosion of sediment is denoted by A . The diffusive transport is characterized by $diff$ and finally convective transport is characterized by $conv$.

The dynamics of the depth-integrated suspended sediment concentration, $\mathcal{C}(t, x, y)$ with unit kg/m^2 , is described by

$$\mathcal{C}_t + \nabla_{xy} \cdot \left[\mathbf{u}\mathcal{C} - \hat{k}_h \left(\nabla_{xy}\mathcal{C} - \frac{\omega_s}{k_v} (\beta_t \nabla_{xy}\zeta - \beta_b \nabla_{xy}h) \mathcal{C} \right) \right] = \alpha \mathbf{u} \cdot \mathbf{u} - \frac{\omega_s^2}{k_v} \beta_b \mathcal{C}, \quad (2.5)$$

where \hat{k}_h is the horizontal eddy diffusivity, k_v the vertical eddy diffusivity, ω_s the settling velocity, α the erosion parameter related to sediment properties, and β_b and β_t are deposition parameters

defined by

$$\beta_b(\zeta, h) \equiv \frac{1}{1 - e^{-\frac{\omega_s}{k_v}(H^I + \zeta - h)}}, \quad (2.6)$$

$$\beta_t(\zeta, h) \equiv e^{-\frac{\omega_s}{k_v}(H^I + \zeta - h)} \beta_b(\zeta, h). \quad (2.7)$$

This equation follows from the conservation of mass, transport and erosion and deposition, assuming that the sediment has a constant grain size of roughly 10^{-4} m. (ter Brake and Schutteleaars (2010))

In Eq. (2.5) the first term on the right describes the erosion of the bed, which is proportional to $\mathbf{u} \cdot \mathbf{u}$. The second term models the deposition of sediment on the bed. The first term on the left describes the local inertia of the suspended sediment concentration. Finally, the second term on the left describes the transport. The transport consists of convective (first term) and diffusive contributions (second, third, and fourth term). The second term is the horizontal diffusion of the depth-integrated sediment concentration, the third and fourth terms capture the diffusive transport related to the vertical structure of the suspended sediment concentration. For details of the derivation starting with the three-dimensional balances, see Appendix B.

Boundary conditions

At the open inlets, the bed height is assumed to be fixed. This means that averaged over a tidal cycle, neither sedimentation nor erosion occurs. This results in the following conditions on the seaward sides:

$$\begin{aligned} \langle \alpha \mathbf{u} \cdot \mathbf{u} - \frac{\omega_s^2}{k_v} \beta_b \mathcal{C} \rangle &= 0, & x = 0, \\ \langle \alpha \mathbf{u} \cdot \mathbf{u} - \frac{\omega_s^2}{k_v} \beta_b \mathcal{C} \rangle &= 0, & x = L. \end{aligned} \quad (2.8)$$

At the north and south boundary conditions, no sediment transport is allowed through these boundaries:

$$\begin{aligned} \left[\mathbf{u} \mathcal{C} - \hat{k} \left(\nabla_{xy} \mathcal{C} - \frac{\omega_s}{k_v} (\beta_t \nabla_{xy} \zeta - \beta_b \nabla_{xy} h) \mathcal{C} \right) \right] \cdot \hat{\mathbf{y}} &= 0, & y = 0, \\ \left[\mathbf{u} \mathcal{C} - \hat{k} \left(\nabla_{xy} \mathcal{C} - \frac{\omega_s}{k_v} (\beta_t \nabla_{xy} \zeta - \beta_b \nabla_{xy} h) \mathcal{C} \right) \right] \cdot \hat{\mathbf{y}} &= 0, & y = B. \end{aligned} \quad (2.9)$$

2.4 Bed evolution

Finally, the evolution of the bed is considered, with $h(t, x, y)$ measured as the distance from H^I , the depth of inlet I . The bed consists of fine sand grains that can move when a large enough force is extended on them. Especially the active layer at the top of the bed is subject to such forces. Sediment can be transported as either bedload or as suspended load. The bedload transport describes the particles that roll, slide, or hop over the bottom. The suspended load transport describes the transport of sediment, with concentration \mathcal{C} , lifted into the fluid. Since the bed evolves slowly in time, only the tidally averaged deposition and erosion result in an appreciable bed change, and the small periodic bed changes within one period are assumed to be negligible. The conservation of mass together with the erosion/deposition gives the following bed evolution equation:

$$\rho_s (1 - p) (h_t - \hat{\mu} \nabla_{xy}^2 h) = - \langle \alpha \mathbf{u} \cdot \mathbf{u} - \frac{\omega_s^2}{k_v} \beta_b \mathcal{C} \rangle, \quad (2.10)$$

where $\nabla_{xy} \equiv \frac{\partial^2}{\partial x^2} + \frac{\partial^2}{\partial y^2}$ denotes the horizontal Laplacian and $\langle \cdot \rangle \equiv \frac{1}{T_{tide}} \int_0^{T_{tide}} \cdot dt$ the tidal average. Furthermore, ρ_s denotes the density of the sediment particles, p the bed porosity and $\hat{\mu}$ is the bed slope parameter, related to the tendency of sediments to roll downhill. In this equation, the first

term denotes the local inertia, followed by the slope term. Finally, the right-hand side of the equation denotes the tidal averaged erosion and deposition.

Boundary conditions

As stated in the earlier, the bed elevation at the seawards boundaries is fixed, resulting in the following boundary conditions:

$$\begin{aligned} h &= H^I, & x &= 0, \\ h &= H^{II}, & x &= L. \end{aligned} \tag{2.11}$$

The no transport conditions of the north and south boundaries read:

$$\begin{aligned} \nabla_{xy} h \cdot \hat{\mathbf{y}} &= 0, & y &= 0, \\ \nabla_{xy} h \cdot \hat{\mathbf{y}} &= 0, & y &= B. \end{aligned} \tag{2.12}$$

3 Solving the model

The focus of this chapter is to introduce the method used to determine the morphologic equilibria of the system of equations derived in chapter 2. The first step is to scale the equations. The second step is to expend the temporal dependency of physical variables in tidal components.

3.1 Scaling the system of equations

Scaling analysis is used to determine the significance of the various terms. The variables are scaled by their typical values making them dimensionless:

$$\begin{aligned} x &= L\tilde{x}, & t &= 2\pi\sigma^{-1}\tilde{t}, & u &= \frac{A_{M_2}^I\sigma L}{H^I}\tilde{u}, & C &= \frac{\alpha U^2}{\omega_s^2/k_v}\tilde{C}, \\ y &= L\tilde{y}, & \zeta &= A_{M_2}^I\tilde{\zeta}, & v &= \frac{A_{M_2}^I\sigma L}{H^I}\tilde{v}, & h &= H^I\tilde{h}. \end{aligned}$$

The variables are denoted by a tilde $\tilde{\cdot}$ are dimensionless. With this scaling the domain under consideration is given by $(\tilde{x}, \tilde{y}) \in [0, 1] \times [0, \frac{B}{L}]$. Time is scaled by the tidal frequency, such that $\tilde{t} = 1$ corresponds to one M_2 period. The velocities are scaled to the typical horizontal velocity $U = \frac{A_{M_2}^I L \sigma}{H^I}$ that follow from continuity. The concentration it is scaled by the ratio between the typical erosion speed and the settling time scale. The bed is scaled to inlet depth at inlet I . The dimensionless system of equations is given by:

$$\nabla_{\tilde{x}\tilde{y}} \cdot \left[(1 + \epsilon\tilde{\zeta} - \tilde{h})\tilde{\mathbf{u}} \right] + \tilde{\zeta}_{\tilde{t}} - \frac{1}{\epsilon}h_{\tilde{t}} = 0, \quad (3.1)$$

$$\tilde{\mathbf{u}}_{\tilde{t}} = -\epsilon[\tilde{\mathbf{u}} \cdot \nabla_{\tilde{x}\tilde{y}}]\tilde{\mathbf{u}} - \lambda_L^{-2}\nabla_{xy}\zeta - \frac{\tilde{r}}{1 + \epsilon\tilde{\zeta} - \tilde{h}}\tilde{\mathbf{u}}, \quad (3.2)$$

$$a \left[\tilde{\zeta}_{\tilde{t}} + \nabla_{\tilde{x}\tilde{y}} \cdot \left(\epsilon\tilde{\mathbf{C}}\tilde{\mathbf{u}} - k(\nabla_{\tilde{x}\tilde{y}}\tilde{\mathbf{C}} - \lambda_d\epsilon\beta_t\nabla_{\tilde{x}\tilde{y}}\tilde{\zeta} + \lambda_d\beta_b\tilde{\mathbf{C}}\nabla_{\tilde{x}\tilde{y}}\tilde{h}) \right) \right] = \tilde{u}^2 + \tilde{v}^2 - \beta_b\tilde{\mathbf{C}}, \quad (3.3)$$

$$\tilde{h}_{\tilde{t}} - \mu\nabla_{\tilde{x}\tilde{y}}^2\tilde{h} = -\delta_s\langle\tilde{u}^2 + \tilde{v}^2 - \beta_b\tilde{\mathbf{C}}\rangle. \quad (3.4)$$

For readability, the tildes are suppressed from now on. The scaled expressions for β_b and β_t are:

$$\beta_b(\zeta, h) \equiv \frac{1}{1 - e^{-\lambda_d(1+\epsilon\zeta-h)}}, \quad (3.5)$$

$$\beta_t(\zeta, h) \equiv e^{-\lambda_d(1+\epsilon\zeta-h)}\beta_b(\zeta, h). \quad (3.6)$$

The dimensionless constants used determine the relative importance of the various terms. The most relevant dimensionless parameter is $\epsilon \equiv \frac{A_{M_2}^I}{H^I}$, the ratio between the depth of the bed and the amplitude of the forcing of the inlet I . All non-linear terms are multiplied with this parameter. The tidal wavelength $\lambda_L \equiv \frac{\sqrt{H^I g}}{L\sigma}$ given by the inverse of the product of the tidal wave number $\frac{\sigma}{\sqrt{gH^I}}$ and the length of the inlet system L . $r \equiv \frac{\hat{r}}{H^I\sigma}$ is the scaled bottom friction constant. a is the time-scaled deposition constant an alternative definition is $a = \frac{\sigma}{\omega_s^2/k_v}$ in the ratio of settling time scale and the tidal time scale, k is the scaled horizontal eddy diffusivity, λ_d is the sediment Peclet number, μ is the bedslope coefficient, δ_s is the ratio of the typical time scale for bed evolution and the tidal period. For the definitions and values of all the dimensionless constants, see table 1.

Table 1: *The dimensionless parameters with their definitions. The final column represents their values specific to the Marsdiep Vlie system.*

Parameter	Definition	Value
ϵ	$\frac{A_{M_2}^I}{H^I} = \frac{U}{L\sigma}$	$6.167 \cdot 10^{-2}$
λ_L	$\frac{\sqrt{H^I g}}{L\sigma}$	1.313
r	$\frac{\hat{r}}{H^I\sigma} = \frac{U}{L\sigma}$	$6.433 \cdot 10^{-1}$
a	$\frac{k_v\sigma}{\omega_s^2}$	$6.222 \cdot 10^{-2}$
k	$\frac{k_h}{L^2\sigma}$	$2.052 \cdot 10^{-4}$
λ_d	$\frac{H^I\omega_s}{k_v}$	1.8
μ	$\frac{\mu}{L^2\sigma}$	$2.873 \cdot 10^{-10}$
δ_s	$\frac{\alpha U^2}{\rho_s(1-p)H^I\sigma}$	$9.533 \cdot 10^{-4}$

In a similar manner, the boundary conditions are scaled, resulting in:

$$\begin{aligned}
\zeta &= \cos(t - \phi^I), & x &= 0, \\
\zeta &= \frac{A^{II}}{A^I} \cos(t - \phi^{II}), & x &= 1, \\
(1 + \epsilon\zeta - h)v &= 0, & y &= 0, \\
(1 + \epsilon\zeta - h)v &= 0, & y &= \frac{B}{L}, \\
u^2 + v^2 - \beta C &= 0, & x &= 0, \\
u^2 + v^2 - \beta C &= 0, & x &= 1, \\
\left[\epsilon \tilde{\mathcal{C}} \tilde{\mathbf{u}} - k(\nabla_{\tilde{x}\tilde{y}} \tilde{\mathcal{C}} - \lambda_d \epsilon \beta_t \nabla_{\tilde{x}\tilde{y}} \tilde{\zeta} + \lambda_d \beta_b \tilde{\mathcal{C}} \nabla_{\tilde{x}\tilde{y}} \tilde{h}) \right] \cdot \hat{\mathbf{y}} &= 0, & y &= 0, \\
\left[\epsilon \tilde{\mathcal{C}} \tilde{\mathbf{u}} - k(\nabla_{\tilde{x}\tilde{y}} \tilde{\mathcal{C}} - \lambda_d \epsilon \beta_t \nabla_{\tilde{x}\tilde{y}} \tilde{\zeta} + \lambda_d \beta_b \tilde{\mathcal{C}} \nabla_{\tilde{x}\tilde{y}} \tilde{h}) \right] \cdot \hat{\mathbf{y}} &= 0, & y &= \frac{B}{L}, \\
h &= 0, & x &= 0, \\
h &= 1 - \frac{H^{II}}{H^I}, & x &= 1, \\
\frac{\partial}{\partial y} h &= 0, & y &= 0, \\
\frac{\partial}{\partial y} h &= 0, & y &= \frac{B}{L}.
\end{aligned} \tag{3.7}$$

3.2 Expansion in tidal components

To solve the dimensionless equations use is made of the observation that $\epsilon \ll 1$. This allows an asymptotic expansion of the physical variables in their small parameters: $\Psi(x, y, t) = \Psi^0(x, y, t) + \epsilon \Psi^1(x, y, t)$ with $\Psi \in \{\zeta, u, v, \mathcal{C}\}$. By substituting the obtained expansions in the system of equations, and ordering, it follows of leading order of the system of equations (3.1) until (3.4) are changed into a system of six partial differential equations that are made easy to solve. Next, this also involves the expansion of the physical variables in the tidal constituent. Next, the time dependency of the ordered variables is captured using a Fourier series in time. Below this the two depth-averaged shallow water equations are expanded. Followed by the expansion of the depth-integrated suspended sediment equation. Finally, the equation to determine the equilibrium bathymetry is derived.

3.2.1 Solving the shallow water equation in tidal components

Assuming the bathymetry does not change over time (so $h(x, t) = h(x)$), the depth-averaged shallow water equation in dimensionless form:

$$\begin{aligned}
\nabla_{xy} \cdot [(1 - h(x, y) + \epsilon\zeta(x, y, t))\mathbf{u}(x, y, t)] + \zeta_t(x, y, t) &= 0, \\
\mathbf{u}_t(x, y, t) &= -\epsilon [\mathbf{u} \cdot \nabla_{xy}] \mathbf{u} - \lambda_L^2 \nabla_{xy} \zeta - \frac{r}{1 - h + \epsilon\zeta} \mathbf{u},
\end{aligned} \tag{3.8}$$

where the double inlet boundary conditions read:

$$\begin{aligned}
\zeta(x, y, t) &= \cos(t), & x &= 0, \\
\zeta(x, y, t) &= \frac{A^{II}}{A^I} \cos(t - \phi_{II}), & x &= 1, \\
[(1 - h(x, y) + \epsilon\zeta(x, y, t))\mathbf{u}(x, y, t)] \cdot \hat{\mathbf{y}} &= 0, & y &= 0 \text{ and } y = \frac{B}{L}.
\end{aligned} \tag{3.9}$$

The physical variables ζ, \mathbf{u} are expand in ϵ as:

$$\begin{aligned}
\zeta(x, y, t) &= \zeta^0(x, y, t) + \epsilon \zeta^1(x, y, t) + \dots, \\
\mathbf{u}(x, y, t) &= \mathbf{u}^0(x, y, t) + \epsilon \mathbf{u}^1(x, y, t) + \dots.
\end{aligned} \tag{3.10}$$

In the following, only the leading order contribution will be considered. A careful analysis of the equations and boundary conditions reveal that, ignoring the transient behaviour, all physical variables only exhibit a periodic behaviour with M_2 time scale.

$$\begin{aligned}\zeta^0(x, y, t) &= \zeta^s(x, y) \sin(t) + \zeta^c(x, y) \cos(t), \\ \mathbf{u}^0(x, y, t) &= \mathbf{u}^s(x, y) \sin(t) + \mathbf{u}^c(x, y) \cos(t).\end{aligned}\tag{3.11}$$

To simplify the notation, the bra-ket notation is used for the temporal part of the physical variables:

$$\sin(t) = |s\rangle, \quad \cos(t) = |c\rangle. \text{ Later, also } \sin(2t) = |2s\rangle \text{ and } \cos(2t) = |2c\rangle \tag{3.12}$$

will be used. The bra-ket notation is defined with the inner product given by $\langle \phi | s \rangle = \frac{1}{\pi} \int_0^{2\pi} \phi(t) \sin(t) dt$. The zeroth-order ϵ expansion of Eqs. (3.8) gives rise to the following linear system of partial differential equations

$$\begin{aligned}\zeta_t^0(x, y, t) &= -\nabla_{xy} \cdot [(1 - h(x, y)) \mathbf{u}^0(x, y, t)], \\ \mathbf{u}_t^0(x, y, t) &= -\lambda_L^2 \nabla_{xy} \zeta^0 - \frac{r}{1 - h} \mathbf{u}^0.\end{aligned}\tag{3.13}$$

Using $\zeta_t^0 = \zeta^s |c\rangle - \zeta^c |s\rangle$ and $\mathbf{u}_t^0 = \mathbf{u}^s |c\rangle - \mathbf{u}^c |s\rangle$ and ortho-normality between $|s\rangle$ and $|c\rangle$. Eq. (3.13) reduces to the following system of equations that describe shallow the shallow water motion:

$$\begin{aligned}\zeta^s &= -\nabla_{xy} \cdot [(1 - h) \mathbf{u}^c], \\ -\zeta^c &= -\nabla_{xy} \cdot [(1 - h) \mathbf{u}^s], \\ \mathbf{u}^s &= -\frac{r}{1 - h} \mathbf{u}^c - \lambda_L^2 \nabla_{xy} \zeta^s, \\ -\mathbf{u}^c &= -\frac{r}{1 - h} \mathbf{u}^s - \lambda_L^2 \nabla_{xy} \zeta^c.\end{aligned}\tag{3.14}$$

The tidal component shallow water boundary conditions read:

$$\begin{aligned}\zeta^s &= 0, & x &= 0, \\ \zeta^c &= 1, & x &= 0, \\ \zeta^s &= A_r \sin(\phi_{II}), & x &= 1, \\ \zeta^c &= A_r \cos(\phi_{II}), & x &= 1, \\ (1 - h)v^s &= 0, & y &= 0, \\ (1 - h)v^c &= 0, & y &= 0, \\ (1 - h)v^s &= 0, & y &= \frac{B}{L}, \\ (1 - h)v^c &= 0, & y &= \frac{B}{L},\end{aligned}\tag{3.15}$$

where $A_r \equiv \frac{A_{II}}{A_I}$.

3.2.2 Solving the sediment concentration in tidal components

The dimensionless depth-integrated concentration equation, Eq. (3.3) reads:

$$a [\mathcal{C}_t + \nabla_{xy} \cdot (\epsilon \mathcal{C} \mathbf{u} - k \nabla_{xy} \mathcal{C} - k \lambda_d \beta \mathcal{C} \nabla_{xy} h)] = \mathbf{u} \cdot \mathbf{u} - \beta \mathcal{C}. \quad (3.16)$$

Because the concentration is forced by the erosion term, the temporal behaviour of the expansion is nontrivial. Up to leading-order accurate ϵ expansion of the depth-integrated concentration equation is given by:

$$0 = -a [\mathcal{C}_t^0 + \nabla_{xy} \cdot (-k \nabla_{xy} \mathcal{C}^0 - k \lambda_d \beta \mathcal{C}^0 \nabla_{xy} h)] + \mathbf{u}^0 \cdot \mathbf{u}^0 - \beta \mathcal{C}^0. \quad (3.17)$$

This leading order equations is forced by the zeroth-order erosion term ($\mathbf{u}^0 \cdot \mathbf{u}^0$). Since the temporal expansion of \mathbf{u}^0 is known, it follows that:

$$\begin{aligned} \mathbf{u}^0 \cdot \mathbf{u}^0 &= \mathbf{u}^s \cdot \mathbf{u}^s |s^2\rangle + 2\mathbf{u}^s \cdot \mathbf{u}^c |sc\rangle + \mathbf{u}^c \cdot \mathbf{u}^c |c^2\rangle, \\ &= \mathbf{u}^s \cdot \mathbf{u}^s \frac{1 - |2c\rangle}{2} + 2\mathbf{u}^s \cdot \mathbf{u}^c \frac{|2s\rangle}{2} + \mathbf{u}^c \cdot \mathbf{u}^c \frac{1 + |2c\rangle}{2}, \\ &= \frac{\mathbf{u}^s \cdot \mathbf{u}^s + \mathbf{u}^c \cdot \mathbf{u}^c}{2} + \mathbf{u}^s \cdot \mathbf{u}^c |2s\rangle + \frac{-\mathbf{u}^s \cdot \mathbf{u}^s + \mathbf{u}^c \cdot \mathbf{u}^c}{2} |2c\rangle, \end{aligned} \quad (3.18)$$

where $|s^2\rangle \equiv \sin(t)^2$ and $|c^2\rangle \equiv \cos(t)^2$. Thus \mathcal{C}^0 has the following orthonormal eigenfunctions: the tidally averaged part ($\langle \mathcal{C} \rangle$) and the M4 tidal part ($|2s\rangle, |2c\rangle$). This gives the following ϵ expansion for $\mathcal{C}(x, y, t)$ up to leading order:

$$\mathcal{C}(x, y, t) = \langle \mathcal{C} \rangle(x, y) + \mathcal{C}^{2s}(x, y) |2s\rangle + \mathcal{C}^{2c}(x, y) |2c\rangle + \mathcal{O}(\epsilon). \quad (3.19)$$

The expressions for the M4 tidal components (\mathcal{C}^{2s} and \mathcal{C}^{2c}) are determined by multiplying equation (3.17) with $\langle 2c|$ or $\langle 2s|$ respectively, and using orthogonality:

$$\begin{aligned} 0 &= -a [2\mathcal{C}^{2s} + \nabla_{xy} \cdot (-k \nabla_{xy} \mathcal{C}^{2c} - k \lambda_d \beta \mathcal{C}^{2c} \nabla_{xy} h)] - \frac{1}{2} \mathbf{u}^s \cdot \mathbf{u}^s + \frac{1}{2} \mathbf{u}^c \cdot \mathbf{u}^c - \beta \mathcal{C}^{2c} \\ 0 &= -a [-2\mathcal{C}^{2c} + \nabla_{xy} \cdot (-k \nabla_{xy} \mathcal{C}^{2s} - k \lambda_d \beta \mathcal{C}^{2s} \nabla_{xy} h)] + \mathbf{u}^s \cdot \mathbf{u}^c - \beta \mathcal{C}^{2s} \end{aligned} \quad (3.20)$$

Finally the expression for the mean tidal contribution $\langle \mathcal{C} \rangle$ is determined by tidally averaging Eq. (3.17):

$$0 = -ak \nabla_{xy} \cdot (-\nabla_{xy} \langle \mathcal{C} \rangle - \lambda_d \beta \langle \mathcal{C} \rangle \nabla_{xy} h) + \frac{1}{2} (\mathbf{u}^s \cdot \mathbf{u}^s + \mathbf{u}^c \cdot \mathbf{u}^c) - \beta \langle \mathcal{C} \rangle. \quad (3.21)$$

Both equations (3.20) and (3.21) are needed to determine the zeroth-order suspended sediment concentration. However, in section 3.2.3 we show that, in leading order only the tidal averaged concentration $\langle \mathcal{C} \rangle$ is needed to determine the equilibrium bathymetry.

The tidally averaged suspended sediment concentration boundary conditions read:

$$\begin{aligned} \frac{1}{2} (u^s u^s + v^s v^s + u^c u^c + v^c v^c) - \beta \langle \mathcal{C} \rangle &= 0, & x = 0 \text{ and } x = 1, \\ [\nabla_{xy} \langle \mathcal{C} \rangle + \lambda_d \beta_b \langle \mathcal{C} \rangle \nabla_{xy} h] \cdot \hat{\mathbf{y}} &= 0, & y = 0 \text{ and } y = \frac{B}{L}. \end{aligned} \quad (3.22)$$

3.2.3 Solving the equilibrium bathymetry

To determine the equilibrium bathymetry a slightly different approach is used. To obtain an equilibrium we require $h(x, y, t) = \langle h(x, y) \rangle$, which directly implies that $\frac{\partial}{\partial t} h(x, y, t) = 0$. Recall the dimensionless bathymetry evolution equation (3.4):

$$\frac{\partial}{\partial t} h(x, y) - \mu \nabla_{xy}^2 h = -\delta_s \langle \mathbf{u} \cdot \mathbf{u} - \beta \mathcal{C} \rangle. \quad (3.23)$$

The tidally averaged erosion $\langle \mathbf{u} \cdot \mathbf{u} \rangle = \frac{1}{2} \mathbf{u}^s \cdot \mathbf{u}^s + \frac{1}{2} \mathbf{u}^c \cdot \mathbf{u}^c$ follows from Eq. (3.14), and the tidally averaged deposition $\langle \mathcal{C} \rangle$ from Eq. (3.21). The equilibrium bathymetry equation follows from requiring:

$$-\mu \nabla_{xy}^2 h = -\delta_s \left(\frac{1}{2} \mathbf{u}^s \cdot \mathbf{u}^s + \frac{1}{2} \mathbf{u}^c \cdot \mathbf{u}^c - \beta \langle \mathcal{C} \rangle \right). \quad (3.24)$$

If $h(x, y)$ satisfies Eq. (3.24) and $\mathbf{u}^s, \mathbf{u}^c$ and $\langle \mathcal{C} \rangle$ satisfy respectively (3.14) and (3.21), the system is in morphodynamic equilibrium and the resulting $h(x, y)$ is the equilibrium bathymetry. Thus \mathcal{C}^{2s} and \mathcal{C}^{2c} are not necessary, therefore they are disregarded.

The boundary conditions read:

$$\begin{aligned} h &= 0, & x &= 0, \\ h &= 1 - \frac{H^{II}}{H^I}, & x &= 1, \\ \frac{\partial}{\partial y} h &= 0, & y &= 0, \\ \frac{\partial}{\partial y} h &= 0, & y &= \frac{B}{L}. \end{aligned} \quad (3.25)$$

3.2.4 System of partial differential equations

The resulting equilibrium solution consists of six variables $\{\zeta^s, \zeta^c, \mathbf{u}^s, \mathbf{u}^c, \langle \mathcal{C} \rangle, h\}$. Here ζ^s, ζ^c represent the tidal components of the water column height, $\mathbf{u}^s, \mathbf{u}^c$ the tidal components of the water flow, $\langle \mathcal{C} \rangle$ the tidal averaged suspended sediment concentration and h the equilibrium bathymetry. The system of six equations of motion that define the equilibrium solution are given by equations (3.14), (3.21) and (3.24). Together they form a solvable system of partial differential equations that do not depend explicitly on time anymore:

$$\begin{aligned}
\zeta^s &= -\nabla_{xy} \cdot [(1-h)\mathbf{u}^c], \\
\zeta^c &= +\nabla_{xy} \cdot [(1-h)\mathbf{u}^s], \\
\mathbf{u}^s &= -\frac{r}{1-h}\mathbf{u}^c - \lambda_L^2 \nabla_{xy} \zeta^s, \\
\mathbf{u}^c &= +\frac{r}{1-h}\mathbf{u}^s + \lambda_L^2 \nabla_{xy} \zeta^c, \\
0 &= ak \nabla_{xy} \cdot (\nabla_{xy} \langle \mathcal{C} \rangle + \lambda_d \beta \langle \mathcal{C} \rangle \nabla_{xy} h) + \frac{1}{2}(\mathbf{u}^s \cdot \mathbf{u}^s + \mathbf{u}^c \cdot \mathbf{u}^c) - \beta \langle \mathcal{C} \rangle, \\
\mu \nabla_{xy}^2 h &= \delta_s \left(\frac{1}{2} \mathbf{u}^s \cdot \mathbf{u}^s + \frac{1}{2} \mathbf{u}^c \cdot \mathbf{u}^c - \beta \langle \mathcal{C} \rangle \right),
\end{aligned} \tag{3.26}$$

with boundary conditions:

$$\begin{aligned}
\zeta^s &= 0, & x &= 0, \\
\zeta^c &= 1, & x &= 0, \\
\zeta^s &= A_r \sin(\phi_{II}), & x &= 1, \\
\zeta^c &= A_r \cos(\phi_{II}), & x &= 1, \\
(1-h)v^s &= 0, & y &= 0 \text{ and } y = \frac{B}{L}, \\
(1-h)v^c &= 0, & y &= 0 \text{ and } y = \frac{B}{L}, \\
\frac{1}{2}(\mathbf{u}^s \cdot \mathbf{u}^s + \mathbf{v}^s \cdot \mathbf{v}^s + \mathbf{u}^c \cdot \mathbf{u}^c + \mathbf{v}^c \cdot \mathbf{v}^c) - \beta \langle \mathcal{C} \rangle &= 0, & x &= 0 \text{ and } x = 1, \\
\frac{\partial}{\partial y} \langle \mathcal{C} \rangle + \lambda_d \beta_b \langle \mathcal{C} \rangle \frac{\partial}{\partial y} h &= 0, & y &= 0 \text{ and } y = \frac{B}{L}, \\
h &= 0, & x &= 0, \\
h &= 1 - \frac{H^{II}}{H^I}, & x &= 1, \\
\frac{\partial}{\partial y} h &= 0, & y &= 0 \text{ and } y = \frac{B}{L}.
\end{aligned} \tag{3.27}$$

4 Numerical method

The system of equations (3.26) found in section 3.2.4, is solved numerically in this chapter. This is done via a multidimensional root-finding algorithm called the Newton-Rapson method. First, the Newton-Rapson method is defined. Next, the model is reshaped in terms of one implicit function. Then this implicit function is discretized and numerically solved. Finally, a method is obtained to determine the stability of equilibrium solutions.

4.1 Newton-Rapson method

Let $\mathbf{f}(\mathbf{x}) : \mathbb{R}^n \rightarrow \mathbb{R}^m$ be a arbitrary multidimensional vector function of which the the roots are desired. Thus \mathbf{x}^* is demanded such that $\mathbf{f}(\mathbf{x}^*) = \mathbf{0}$. Assume that the current \mathbf{x} is a close enough approximation of the desired root \mathbf{x}^* . Let $\delta\mathbf{x}$ be removed from \mathbf{x}^* than $\mathbf{f}(\mathbf{x} + \delta\mathbf{x}) = 0$. The second-order Taylor expansion gives:

$$\mathbf{f}(\mathbf{x} + \delta\mathbf{x}) = \mathbf{f}(\mathbf{x}) + \nabla\mathbf{f}(\mathbf{x})\delta\mathbf{x} + \mathcal{O}(\delta\mathbf{x}^2).$$

Here $\nabla\mathbf{f}$ describes the Jacobian matrix of \mathbf{f} also denoted as $[J](\mathbf{x})$. This gives an approximation for $\delta\mathbf{x}$ if \mathbf{x} is close enough, namely:

$$\delta\mathbf{x} = -[J](\mathbf{x})^{-1}\mathbf{f}(\mathbf{x}).$$

If the system converges than $\delta\mathbf{x}$ points in the direction of the desired root. Thus with a sufficiently accurate initial guess \mathbf{x}_0 the Newton-Rapson method can be used in the following iterative way:

$$\mathbf{x}_{n+1} = \mathbf{x}_n + \delta\mathbf{x}_n = \mathbf{x}_n - [J](\mathbf{x}_n)^{-1}\mathbf{f}(\mathbf{x}_n).$$

This iteration is stopped when for the N th iteration the norm $\|\mathbf{f}(\mathbf{x}_N)\|$ is smaller than a pre set value ϵ : $\|\mathbf{f}(\mathbf{x}_N)\| < \epsilon$. Where $\|\cdot\|$ denotes the 2 norm.

4.2 Restating as an implicit function

Because the Newton-Rapson method finds the roots of implicit functions, the system of equations (3.26) must be restated as an implicit function $\mathbf{f}(\mathbf{x})$ such that its roots give the morphodynamical equilibrium solution. In this case the variables are defined by $\mathbf{x} = [\zeta^s \ \zeta^c \ u^s \ u^c \ v^s \ v^c \ \langle\mathcal{C}\rangle \ h]^T$. Here $\mathbf{f}(\mathbf{x})$ reads:

$$\mathbf{0} = \mathbf{f}(\mathbf{x}) = \begin{cases} 0 = -\zeta^s - (1-h)(\frac{\partial}{\partial x}u^c + \frac{\partial}{\partial u}v^c) + u^c\frac{\partial h}{\partial x} + v^c\frac{\partial h}{\partial y}, \\ 0 = -\zeta^c + (1-h)(\frac{\partial}{\partial x}u^s + \frac{\partial}{\partial u}v^s) - u^s\frac{\partial h}{\partial x} - v^s\frac{\partial h}{\partial y}, \\ 0 = -u^s - \frac{r}{1-h}u^c - \lambda_L^2\frac{\partial}{\partial x}\zeta^s, \\ 0 = -u^c + \frac{r}{1-h}u^s + \lambda_L^2\frac{\partial}{\partial x}\zeta^c, \\ 0 = -v^s - \frac{r}{1-h}v^c - \lambda_L^2\frac{\partial}{\partial y}\zeta^s, \\ 0 = -v^c + \frac{r}{1-h}v^s + \lambda_L^2\frac{\partial}{\partial y}\zeta^c, \\ 0 = \mathbf{f}_{\langle\mathcal{C}\rangle}(\mathbf{x}), \\ 0 = \mathbf{f}_h(\mathbf{x}), \end{cases} \quad (4.1)$$

with the suspended sediment concentration constraint is given by:

$$\begin{aligned} \mathbf{f}_{\langle\mathcal{C}\rangle}(\mathbf{x}) = & ak \left(\frac{\partial^2 \langle\mathcal{C}\rangle}{\partial x^2} + \frac{\partial^2 \langle\mathcal{C}\rangle}{\partial y^2} + \lambda_d \left[\langle\mathcal{C}\rangle \left(\frac{\partial\beta}{\partial x}\frac{\partial h}{\partial x} + \frac{\partial\beta}{\partial y}\frac{\partial h}{\partial y} \right) + \beta \left(\frac{\partial\langle\mathcal{C}\rangle}{\partial x}\frac{\partial h}{\partial x} + \frac{\partial\langle\mathcal{C}\rangle}{\partial y}\frac{\partial h}{\partial y} \right) + \langle\mathcal{C}\rangle\beta \left(\frac{\partial^2 h}{\partial x^2} + \frac{\partial^2 h}{\partial y^2} \right) \right] \right) \\ & + \frac{1}{2} (u^s u^s + u^c u^c + v^s v^s + v^c v^c) - \beta \langle\mathcal{C}\rangle, \end{aligned} \quad (4.2)$$

and the equilibrium bathymetry is constrained by:

$$\mathbf{f}_h(\mathbf{x}) = \mu \left(\frac{\partial^2 h}{\partial x^2} + \frac{\partial^2 h}{\partial y^2} \right) - \delta_s \left(\frac{1}{2} (u^s u^s + u^c u^c + v^s v^s + v^c v^c) - \beta \langle\mathcal{C}\rangle \right). \quad (4.3)$$

It is found that the quadratic (erosion) term in Eq. (4.1) term introduces large numerical inaccuracies. This problem is solved by using Eq. (4.2) and rewriting the erosion deposition term as sediment transport, resulting in the following equilibrium bathymetry constraint:

$$\mathbf{f}_h(\mathbf{x}) = \mu \left(\frac{\partial^2 h}{\partial x^2} + \frac{\partial^2 h}{\partial y^2} \right) + \delta_s a k \left(\frac{\partial^2 \langle \mathcal{C} \rangle}{\partial x^2} + \frac{\partial^2 \langle \mathcal{C} \rangle}{\partial y^2} + \lambda_d \left[\langle \mathcal{C} \rangle \left(\frac{\partial \beta}{\partial x} \frac{\partial h}{\partial x} + \frac{\partial \beta}{\partial y} \frac{\partial h}{\partial y} \right) + \beta \left(\frac{\partial \langle \mathcal{C} \rangle}{\partial x} \frac{\partial h}{\partial x} + \frac{\partial \langle \mathcal{C} \rangle}{\partial y} \frac{\partial h}{\partial y} \right) + \langle \mathcal{C} \rangle \beta \left(\frac{\partial^2 h}{\partial x^2} + \frac{\partial^2 h}{\partial y^2} \right) \right] \right). \quad (4.4)$$

4.3 Discretization

It is not possible to solve equation (4.1) analytically. Therefore numerical methods are used. First, the domain $[0, 1] \times [0, \frac{B}{L}]$ is discretized in $(N_x + 2) \times (N_y + 2)$ grid points. Here N_x and N_y denote the number of interior grid points. The values of the variables are stored in the lexicographically ordered vectors called $\boldsymbol{\zeta}^s, \boldsymbol{\zeta}^c, \mathbf{u}^s, \mathbf{u}^c, \mathbf{v}^s, \mathbf{v}^c, \mathbf{C}, \mathbf{h}$. In this discretization the partial derivative $\frac{\partial}{\partial x}$ becomes the central difference matrix $[L_x]$. Similarly $\frac{\partial}{\partial y}$ becomes $[L_y]$. The second order derivative $\frac{\partial^2}{\partial x^2}$ becomes the finite difference second order derivative matrix $[L_{xx}]$. Similarly $\frac{\partial^2}{\partial y^2}$ becomes $[L_{yy}]$. The discrete shallow water constraint derived by the discretization of Eq. (4.1) and is on the interior of the domain given by:

$$\begin{aligned} \mathbf{f}_{\zeta^s} &= -\boldsymbol{\zeta}^s - (1 - \mathbf{h}) \circ ([L_x] \mathbf{u}^c + [L_y] \mathbf{v}^c) + \mathbf{u}^c \circ [L_x] \mathbf{h} + \mathbf{v}^c \circ [L_y] \mathbf{h}, \\ \mathbf{f}_{\zeta^c} &= -\boldsymbol{\zeta}^c + (1 - \mathbf{h}) \circ ([L_x] \mathbf{u}^s + [L_y] \mathbf{v}^s) - \mathbf{u}^s \circ [L_x] \mathbf{h} - \mathbf{v}^s \circ [L_y] \mathbf{h}, \\ \mathbf{f}_{u^s} &= -\mathbf{u}^s - \frac{r}{1 - \mathbf{h}} \circ \mathbf{u}^c + \lambda_L^2 [L_x] \boldsymbol{\zeta}^s, \\ \mathbf{f}_{u^c} &= -\mathbf{u}^c + \frac{r}{1 - \mathbf{h}} \circ \mathbf{u}^s - \lambda_L^2 [L_x] \boldsymbol{\zeta}^c, \\ \mathbf{f}_{v^s} &= -\mathbf{v}^s - \frac{r}{1 - \mathbf{h}} \circ \mathbf{v}^c - \lambda_L^2 [L_y] \boldsymbol{\zeta}^s, \\ \mathbf{f}_{v^c} &= -\mathbf{v}^c + \frac{r}{1 - \mathbf{h}} \circ \mathbf{v}^s + \lambda_L^2 [L_y] \boldsymbol{\zeta}^c. \end{aligned} \quad (4.5)$$

Here \circ denotes the Hadamard product. The discrete constraints for the equilibrium concentration profile reads:

$$\begin{aligned} \mathbf{f}_{\mathbf{C}} &= ak ([L_{xx}] \mathbf{C} + [L_{yy}] \mathbf{C} + \lambda_d [\mathbf{C} \circ ([L_x] \boldsymbol{\beta} \circ [L_x] \mathbf{h} + [L_y] \boldsymbol{\beta} \circ [L_y] \mathbf{h}) + \boldsymbol{\beta} \circ ([L_x] \mathbf{C} \circ [L_x] \mathbf{h} + [L_y] \mathbf{C} \circ [L_y] \mathbf{h}) \\ &\quad + \mathbf{C} \circ \boldsymbol{\beta} \circ ([L_{xx}] \mathbf{h} + [L_{yy}] \mathbf{h}) + \frac{1}{2} (\mathbf{u}^s \circ \mathbf{u}^s + \mathbf{u}^c \circ \mathbf{u}^c + \mathbf{v}^s \circ \mathbf{v}^s + \mathbf{v}^c \circ \mathbf{v}^c) - \boldsymbol{\beta} \circ \mathbf{C}). \end{aligned} \quad (4.6)$$

Note that $\boldsymbol{\beta}$ is a function of h thus $\boldsymbol{\beta}(h)$ becomes a lexicographical vector $\boldsymbol{\beta}$. The discrete equilibrium bathymetry constraints read:

$$\begin{aligned} \mathbf{f}_{\mathbf{h}} &= \mu ([L_{xx}] \mathbf{h} + [L_{yy}] \mathbf{h}) + \delta_s ak ([L_{xx}] \mathbf{C} + [L_{yy}] \mathbf{C} \\ &\quad + \lambda_d [\mathbf{C} \circ ([L_x] \boldsymbol{\beta} \circ [L_x] \mathbf{h} + [L_y] \boldsymbol{\beta} \circ [L_y] \mathbf{h}) + \boldsymbol{\beta} \circ ([L_x] \mathbf{C} \circ [L_x] \mathbf{h} + [L_y] \mathbf{C} \circ [L_y] \mathbf{h}) \\ &\quad + \mathbf{C} \circ \boldsymbol{\beta} \circ ([L_{xx}] \mathbf{h} + [L_{yy}] \mathbf{h})], \end{aligned} \quad (4.7)$$

where the boundaries are prescribed in Appendix C.

4.4 Jacobian

The Jacobian matrix $[J](\boldsymbol{\zeta}^s, \boldsymbol{\zeta}^c, \mathbf{u}^s, \mathbf{u}^c, \mathbf{v}^s, \mathbf{v}^c, \mathbf{C}, \mathbf{h})$ is dependent on the variables since \mathbf{f} is non-linear. This matrix can be determined analytically, but this is a tedious job. Instead, each submatrix is calculated numerically with spacing $h = 10^{-12}$, the results are stored in sparse matrices $[J]$. As most values of the Jacobian are zero the sparsity of the matrix greatly reduces the data required to store the large number of values of the model. The python function `scipy.sparse.linalg.solve()` is used to determine each step of the Newton-Raphsons algorithm. Combining this with a sufficiently accurate initial guess the Newton-Raphson algorithm allow for determining morphodynamic equilibria.

4.5 Stability analysis

A morphodynamic equilibrium solution $\mathbf{f}(\mathbf{x}^*) = 0$ is called (asymptotically) stable if after every small perturbation the system returns to the same equilibrium solution \mathbf{x}^* . Conversely, a point \mathbf{x} is called unstable if there exists at least one tiny perturbation that does not return to \mathbf{x} . The multi-dimensional function \mathbf{f} is stable if and only if all eigenvalues of the Jacobian matrix $[J](\mathbf{x})$ compose of a negative real part.

To determine the largest real eigenvalue of $[J]$ the shifted power method is used as stated in Vuik and Lahaye (2019). The power method is one of the most straightforward methods for finding the eigenvalue with the largest magnitude. Since the Jacobian $[J]$ is a normal matrix it follows that the eigenvalues can be ordered as $\lambda_1 \geq \lambda_2 \geq \dots \geq \lambda_n$.

To calculate the largest real eigenvalue, the power method is shifted in the following way: Assume that $\lambda_1 > \lambda_2 > \dots > \lambda_N$, then λ_1 can be determined by the power method. Now, consider a new shifted system $[\tilde{J}] = [J] + \lambda_1[I]$ where $[I]$ is the identity matrix. For this new shifted system the largest eigenvalue μ_N defined as $\mu_N \mathbf{v}_N = [\tilde{J}] \mathbf{v}_N = ([J] + \lambda_1[I]) \mathbf{v}_N = (\lambda_N + \lambda_1) \mathbf{v}_N$ is given by the power method. Now the largest eigenvalue is given by $\lambda_N = \mu_N - \lambda_1$.

5 Results and Discussion

To interpret the results obtained with the model, these results are compared with observations of the Marsdiep Vlie system in the Dutch Wadden Sea (see figure 1). First, the system-specific parameter values are given. Next, a typical equilibrium solution is analysed physically and its characteristics summarized. Then the sensitivity of these characteristics is tested by variation of inlet parameters. Finally, the stability of the width-averaged equilibrium solutions is tested in the extended two-dimensional model.

5.1 Parameter values of the Marsdiep Vlie system

As stated earlier, the Marsdiep Vlie domain has length $L = 60 \cdot 10^3$ m and width $B = 1 \cdot 10^3$ m. The values of the parameter constants used in this model are summarized in Tab. 2.

Table 2: *The values of these parameters origin from Deng et al. (2020)*

System				Inlets			
channel length	L	$60 \cdot 10^3$	m	sea level at inlet I	H^I	11.7	m
channel width	B	$1 \cdot 10^3$	m	sea level at inlet II	H^{II}	11.9	m
gravitational acceleration	g	9.81	m s^{-2}	amplitude of the M_2 tide	$A_{M_2}^I$	0.62	m
drag coefficient	c_d	0.0025	—	amplitude of the M_2 tide	$A_{M_2}^{II}$	0.77	m
Tidal M_2 period	T	$44.9 \cdot 10^3$	s	phase of the M_2 tide	$\phi_{M_2}^I$	0°	—
				phase of the M_2 tide	$\phi_{M_2}^{II}$	54°	—

Sediment				Bed			
horizontal diffusivity	\hat{k}_h	10^2	$\text{m}^2 \text{s}^{-1}$	sediment density	ρ_s	2650	kg m^{-3}
vertical diffusivity	k_v	0.1	$\text{m}^2 \text{s}^{-1}$	bed porosity	p	0.4	—
settling velocity	ω_s	0.015	m s^{-1}	bed slope coefficient	$\hat{\mu}$	$1.4 \cdot 10^{-4}$	$\text{m}^2 \text{s}^{-1}$
erosion parameter	α	$0.5 \cdot 10^{-2}$	kg s m^{-4}				

Practical simplification of the model

To be able to obtain solutions within a practical computation time simplifications were needed. In equations (4.6) and (4.7) the suspended sediment transport compensation for topological changes has nonlinear dependencies on the central difference matrices $[L_x]$ and $[L_y]$. Specifically, in equations (4.7) the slope term is of order 10^{-10} and the sediment transport terms are of order 10^{-9} . In the vertical compensation of the transport term, the central difference matrix is used, which can cause some singularity perturbation problems, especially since the dependencies are nonlinear. This tends to create complications, especially using this in large nonlinear terms can create convergence problems. So to help increase the rate of convergence, the suspended sediment transport is assumed to be dominated by diffusion, thus transport compensations by topological changes are neglected. As a consequence equations (4.6) and (4.7) simplify to:

$$\begin{aligned}
 \mathbf{f}_C &= ak ([L_{xx}]\mathbf{C} + [L_{yy}]\mathbf{C}) + \frac{1}{2} (\mathbf{u}^s \circ \mathbf{u}^s + \mathbf{u}^c \circ \mathbf{u}^c + \mathbf{v}^s \circ \mathbf{v}^s + \mathbf{v}^c \circ \mathbf{v}^c) - \beta \circ \mathbf{C}, \\
 \mathbf{f}_h &= \mu ([L_{xx}]\mathbf{h} + [L_{yy}]\mathbf{h}) + \delta_s ak ([L_{xx}]\mathbf{C} + [L_{yy}]\mathbf{C}).
 \end{aligned} \tag{5.1}$$

This simplification helps increase the rate of convergence of the equilibrium solutions, making the computational time for normal hardware more practical.

5.2 Typical solution analysis

To understand the model better, one-dimensional results are analysed first. The model becomes one-dimensional by reducing the transverse discretization to one internal point ($N_y = 1$). All results are obtained by using sixty internal points in the longitudinal direction ($N_x = 60$). The numerical method converges only if the initial guess is 'close enough'. Therefore, a simpler system is initially considered. The system considered has equal undisturbed water depth at both inlets ($H^I = H^{II}$) and incoming waves with identical amplitudes ($A^I = A^{II}$) but with a 90 phase difference ($\Delta\phi = 90^\circ$). So when inlet I is at maximum tide the water level at inlet II is exactly halfway.

The resulting equilibrium width-averaged undisturbed water depth is shown in figure 4. The skewed parabolic bathymetry has a minimum water depth of 10.32 m near the centre of the channel. The most important value is the minimal water depth as the system becomes clogged if this becomes zero. The M_2 water level variation is shown in figure 5a and in figure, 5b describes the water for both the sine and cosine both tidal components. During an M_2 tidal cycle, four distinct water levels are distinguished, high tide, ebb tide, low tide, and flood tide.

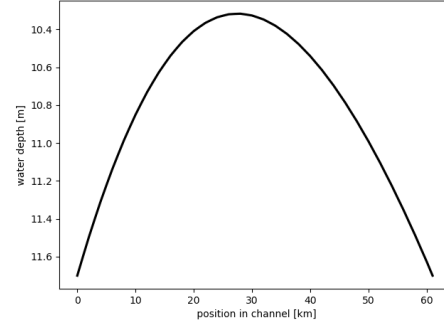
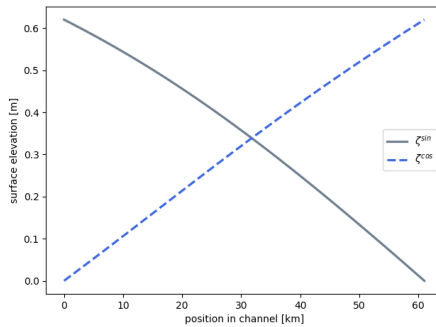
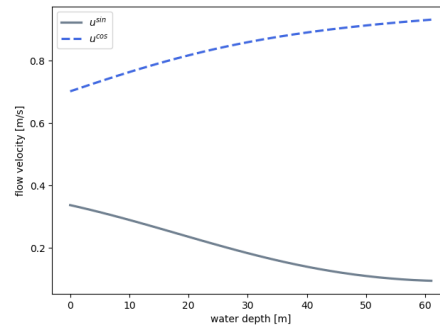


Figure 4: Width averaged bathymetry expressed in the undisturbed water depth for the initial system. With a minimal water depth of 10.32 m.

- High tide: $u = u^{\cos}$ and $\zeta = \zeta^{\cos}$. Zero flow at inlet I .
- Ebb tide: $u = u^{\sin}$ and $\zeta = \zeta^{\sin}$. Maximal flow at inlet I .
- Low tide: $u = -u^{\cos}$ and $\zeta = -\zeta^{\cos}$. Zero flow at inlet I .
- Flood tide: $u = -u^{\sin}$ and $\zeta = -\zeta^{\sin}$. Maximal negative flow at inlet I .



(a)



(b)

Figure 5: M_2 water motion of the simplified system.

(a) Width averaged water level in tidal components.

(b) The amplitude of the tidal components of the water flow.

In both (a) and (b) the dotted line represents the 'high tide' component and the solid line the 'ebb tide' component.

In figure 5b it can be observed that the high tide water velocity at inlet I is 0.72 m/s and increases to 0.93 m/s at inlet II . Since the velocities at both inlets have identical signs, it becomes clear

that at high tide water in through Marsdiep inlet and out via the Vlie inlet. The maximal water flow during one M_2 period is a measure of erosion. The most important morphodynamical impact of the water flow is the erosion of the bed. If at someplace in the bed there is no erosion, then the bed quickly rises due to deposition. Therefore, the minimum of the maximal water flow becomes important to track and thus it is a characteristic. From 5b follows that the characteristic flow of this equilibrium is 0.78 m/s. The sediment behaviour is shown in figure 6. The suspended sediment concentration is shown in figure 6a and the sediment transport is displayed in figure 6b.

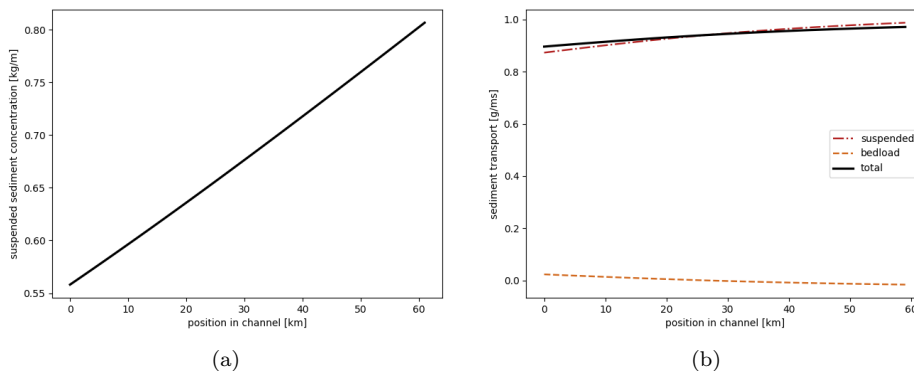


Figure 6:

- (a) Suspended sediment concentration in the channel.
(b) The various sediment transport contributions. The dot-dashed line represents the suspended sediment transport, the dashed line represents the bedload transport and the solid line represents the total transport.

In figure 6b it can be seen that the mean sediment transport in the system is $0.97 \frac{\text{g}}{\text{m s}}$. The large water velocities give rise to the high suspended sediment concentration seen in figure 6a. Consequently, the dominant transport phenomenon is the diffusion. The parabolic profile of the bathymetry can be understood from the sediment transport in figure 6b together with equation (4.4). Figure 6a suggests that the tidally averaged sediment concentration increases linearly. However, if this would be the case than substituting this in equation (4.4) reveals that the bathymetry must then also increase linearly, this contradicts the observations. However, if $\langle C \rangle$ is estimated as a quadratic function. Than, substituting this in equation (4.4) gives that the one-dimensional bed topology $h(x)$ should be parabolic. Exactly as observed in 4.

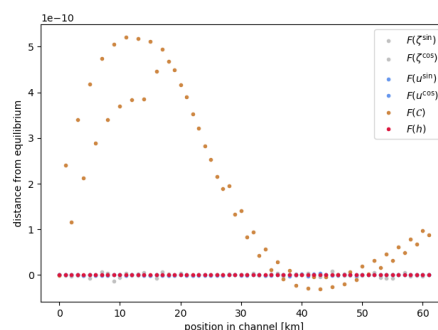


Figure 7: The accuracy of the equilibrium solution. The tidal averaged suspended sediment concentration has the lowest accuracy.

The numerical method continues until this solution deviates maximally $1 \cdot 10^{-8}$ from the 'true' equilibrium solution. This is called the accuracy of the equilibrium and it is tested via the implicit function $\mathbf{0} = \mathbf{f}(\mathbf{x})$ stated in equation (3.14). The accuracy per variable can be seen in figure 7. However, the difference in accuracy per variable has no meaning as the entire system is cross-dependent. Thus the accuracy of an equilibrium solution is equal to the lowest accuracy of all physical quantities in this equilibrium, which lead to $5.69 \cdot 10^{-9}$.

An equilibrium solution can be characterized by specific parameters. These characterizations are needed to help understand the changes of the equilibrium during the next experiments. The characteristics of this system are:

- Characteristic depth: the minimum water depth, here 10.32 m,
- Characteristic flow: the minimum of the maximum water velocity for all locations in the estuary achieved during one M_2 period, here 0.78 m/s,
- Characteristic transport: the direction and magnitude of the mean sediment transport $0.97 \frac{\text{g}}{\text{m s}}$.

5.3 Variation of parameters.

To test the behaviour of the system, the following variation of system parameters are considered: phase ($\Delta\phi$), incoming M_2 wave amplitudes (A_r) and inlet depth (H^{II}/H^I). The first experiment varies the phase while the other parameters are fixed. The following experiment varies the wave amplitudes. The final experiment varies the water depth. During each experiment, the equilibria are analysed by their characteristics and the bed topology as a function of the changing parameter.

5.3.1 Variation of tidal phase difference experiment.

The distance that the M_2 wave needs to travel via the open sea between inlet I and II determines the phase difference between the waves at the inlets. If the inlets are located very close to each other, the phase difference tends to zero. When the phase difference is decreased, starting at 90° the waves oppose each other increasingly. This results in a decrease of the water flow that in turn results in a decrease of the erosion. As a consequence, the channel becomes shallower. The different width-averaged bathymetries as a variation of phase difference are shown in figure 8.

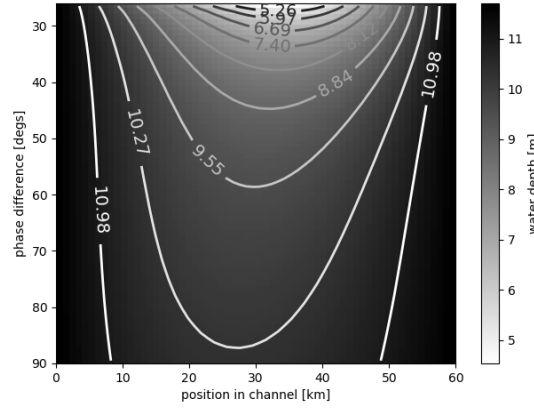


Figure 8: *Equilibrium water depth a under variation of ϕ from 90° to 26° . The shade denotes the water depth. White represents the shallowest channel depth and black represents the deepest channel depth.*

In figure 8 it can be seen that the 10.32 m deep skewed parabolic bathymetry seen in figure 4 at $\Delta\phi = 90^\circ$ changes to a bed that is maximally 5.4 m deep at $\Delta\phi = 26^\circ$. However, decreasing the phase difference further does not result in an equilibrium: at a phase of 26° a limit point bifurcation is found and it was found that for $\Delta\phi \in (26^\circ, 0^\circ)$ no solution exists. The reason for this is that the only possible solution that exists in this region has a zero water depth at some point in the channel and thus the only solution is a clogged channel. The characteristics are shown in figure 9. The minimal water depth increases very quickly nearing the bifurcation point with the minimum water depth of 5.4 m. The lowest maximal water flow before the channel becomes clogged is 0.23 m/s. Furthermore, the characteristic water velocity decreases linearly until 56° then it decreases even quicker until the limit point bifurcation. The mean sediment transport decreases below zero to end up at $-0.15 \frac{\text{g}}{\text{m s}}$ at the limit point bifurcation, indicating that the net sediment transport is from inlet II to inlet I .

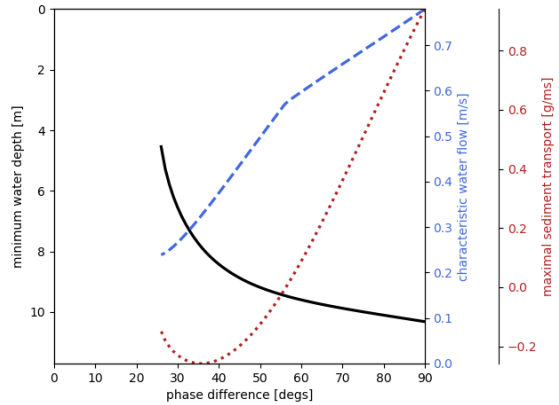


Figure 9: *Equilibrium characteristics under the variation of ϕ from 90° to 26° . Here the solid line together denotes the minimum depth. The dashed line denotes the lowest maximum water flow. The dotted line denotes the mean sediment transport.*

The complex behaviour close to the limit point bifurcations can be understood using dynamical systems theory, but this suppresses the scope of this thesis. The observed results are in accordance with the results found in Deng et al. (2020). In this thesis a different model and method are used, so encountering similar behaviour strengthens the limit point bifurcation theory. However, to fully explore these limit point bifurcations exceeds the scope of this project. For more information about limit point bifurcations in double inlet systems see Deng et al. (2020).

5.3.2 Variation of incoming wave amplitude.

The M_2 tidal wave amplitude varies depending on the geometry of the sea. To capture this, an experiment with different wave amplitude ratios is necessary. The ratio between the amplitude of the incoming waves is defined as A_r , where we have that $A^{II} = A_r \cdot A^I$. The system characteristics and bed topologies as a result of the varying amplitude ratio are shown in figure 10.

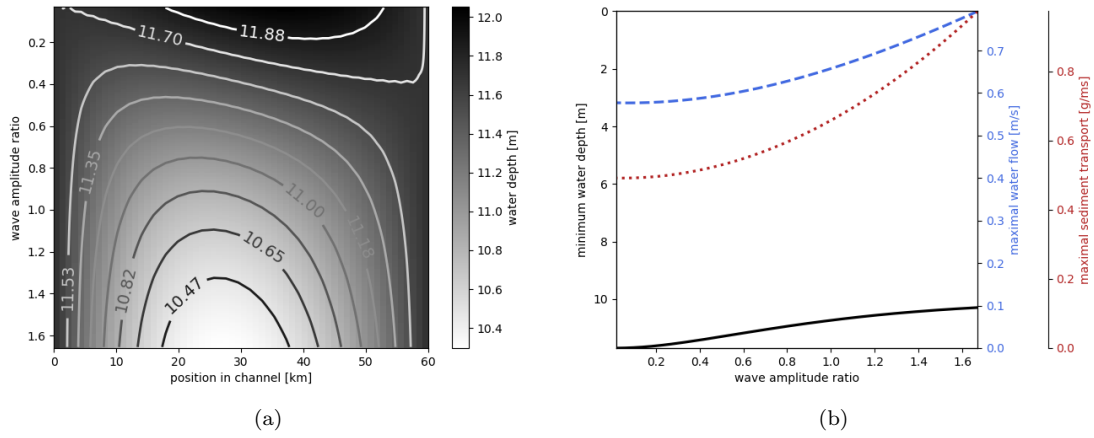


Figure 10: *Equilibrium profiles under variation of A_r from 0.02 to 1.67.*

(a) *the bathymetry as a function of channel position and varied parameter*

(b) *Equilibrium characteristics here the solid line together denotes the minimum water depth. The dashed line denotes the maximum water flow. The dotted line denotes the maximal sediment transport.*

From figure 10 it becomes clear that the bed topology becomes shallower if $A^{II} > A^I$ and becomes deeper if $A^{II} < A^I$. Figure 10a shows that the bed topology remains relatively flat, the maximum difference between deepest and shallowest point does not exceed 1.2 m. The equilibrium characteristics in figure 10b reinstate that varying the incoming wave amplitude does nothing drastic to the morphological equilibria the system. Even if A^{II} is 1.6 times larger than A^I the water depth reduces only by roughly 1 m. There are no drastic changes and the system does not encounter any limit point bifurcations. Note that these graphs only hold for $\Delta\phi = 90^\circ$ and $H^I = H^{II}$.

5.3.3 Variation of inlet depth.

The seaward inlet water depth can change due to external forces and human interventions or due to morphodynamical changes of larger systems caused by global warming. To examine the effect of a change in inlet water depth, an experiment is carried out in which the ratio between inlet depth is varied and analysed. We define the inlet depth ratio between the water depth H^I at inlet I and water depth H^{II} at inlet II as $H_r \equiv \frac{H^{II}}{H^I}$. The changes in bed topology as a result of varying inlet depth ratio are shown in figure 11.

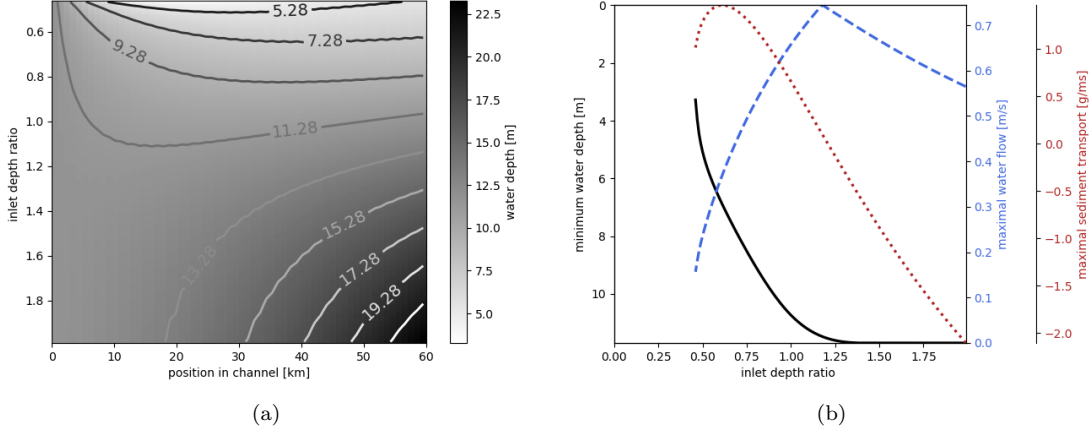


Figure 11: *Equilibrium water depth under variation of H_r from 0.48 to 2.*

(a) *The bathymetry as a function of channel position and varied parameter*

(b) *Equilibrium characteristics, here the solid line together denotes the minimum water depth. The dashed line denotes the maximum water flow. The dotted line denotes the maximal sediment transport.*

From figure 11 it follows that a deep H^{II} relative to H^I creates no complications. However, increasing H^{II} creates interesting characteristics. The characteristic water flow peaks at $H_r = 1.18$ with a maximum flow of 0.77 m/s. After this, the characteristic flow quickly drops to 0.16 m/s before reaching a limit point bifurcation. An explanation for this behaviour can be identified if this system is compared with a nozzle system. In the case that $H^{II} > H^I$ the area at inlet II is larger than that of area I . Since water is a conserved quantity the velocity at inlet II becomes minimal. Similarly, when $H^{II} < H^I$ the lowest velocity is measured at inlet I . The difference between the two cases is that when $H^{II} < H^I$ the channel depth remains constantly H^{II} for roughly 30 km. Consequently, the 'nozzle' becomes shorter and thus the minimal velocity becomes smaller. When $H^{II} \approx H^I$, the system resembles a straight pipes and thus the maximum tidal velocity should become homogeneous everywhere in the channel. However, when $H_r = 1$ the bathymetry is parabolic (as seen in figure 4). Therefore, the maximum characteristic flow is not exactly at $H_r = 1$ but at $H_r = 1.18$. As the characteristic flow decreases from $H_r = 1.18$ the minimum water depth suddenly increases to reach the shallowest depth before the limit point bifurcation of 3.97 m at $H_r = 0.46$. The characteristic sediment transport changes sign at exactly when the characteristic flow turns to peak at 1.48 g/ms at $H_r^{II} = 0.6$. After this, the characteristic transport decreases to 1.13 g/ms at the limit point bifurcation.

5.4 Stability of the width-averaged equilibrium solutions in two dimensions.

To be able to analyze if the complicated width-averaged behaviour of double inlet systems, as shown in the previous three experiments, is stable in the two-dimensional extended model, two questions must be answered: Are the width-averaged equilibria also equilibria in the extended model? Are the width-averaged equilibria stable in the extended model? Since that stability of the width-averaged equilibria are tested, $N_y = 3$ suffices, additionally, this keeps the computing time practical.

Accuracy of width-averaged solutions in the extended model

The accuracies of the width-averaged equilibria in the extended model are tested using the implicit function stated in equation (3.14). The accuracy of the equilibria in the non-extended model is all less than 10^{-8} as this was the stop condition for the numerical method. The accuracies of the width-averaged equilibria in the extended model are shown in figure 12.

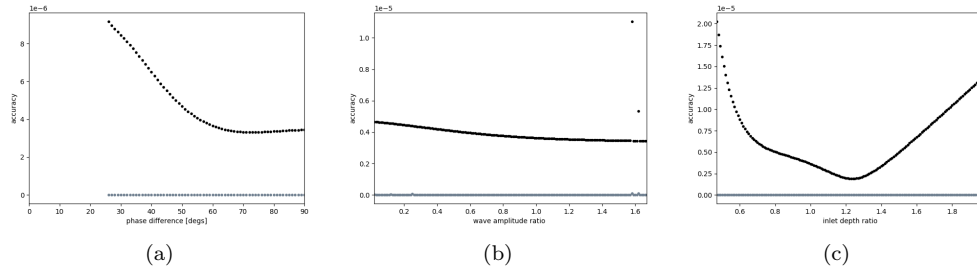


Figure 12: The accuracies of the three experiments, where black points represent the accuracy in the extended model and the gray points represent the accuracy in the width-averaged model.

- (a) The accuracy of the equilibrium solutions under variation of phase difference.
- (b) The Accuracy of the equilibrium solutions under variation of tidal wave amplitude.
- (c) The Accuracy of the equilibrium solutions under variation of inlet depth.

In figure 12 it can be seen that the accuracy of the width-averaged model has decreased to 10^{-5} . The reason for this is that the horizontal bedload and sediment transport tend to create curved surfaces, however, the accuracy is still four orders smaller than the order of the lowest measured quantity, so these solutions are still quite good approximations of the equilibrium solutions. Additionally, in figures 12a and 12c it can be seen that close to the limit point bifurcations the accuracy drastically increases. Therefore, it is possible that close to the limit point bifurcations, the system is forced to leave the width-averaged equilibrium to try to remain stable by expressing itself in quantities that vary over the width of the channel.

Stability of width-averaged solutions in the extended model

To analyse the stability of the width-averaged equilibrium solutions in the extended model, the eigenvalues are calculated. The eigenvalues of the solutions in the extended and nonextended models are shown in figure 13.

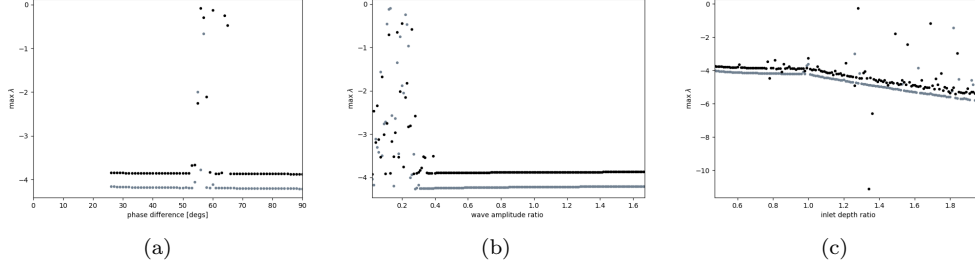


Figure 13: *The largest eigen values of the width-averaged equilibrium solutions in the extended (black) and non-extended (gray) under variation of parameters.*

- (a) *The eigen values of the equilibrium solutions under variation of phase difference.*
- (b) *The eigen values of the equilibrium solutions under variation of tidal wave amplitude.*
- (c) *The eigen values of the equilibrium solutions under variation of inlet depth.*

In figure 13 it can be seen that for each equilibrium solution in both the extended and not extended model, the largest eigenvalue is negative. This is strong evidence that the width-averaged equilibria form stable equilibria in the two-dimensional extended model. However, the significant number of discontinuities seen in figures 13a and 13b of the eigenvalues of both models suggest that something is off, as in general, the eigenvalues should change continuously under variations of parameters. This could be a result of minor resolution errors adding up in such a large system or a modelling mistake in some not important variables. Note that no aberrant behaviour is visible for the equilibria with discontinuous eigenvalues in figures 8 and 10a. In figure 13c it can be seen that the further the parameters are from the limit point bifurcation, the more negative the largest eigenvalues become. Moreover, it can be observed that the eigenvalues in the extended model are less negative than in the non-extended model. However, that the eigenvalues of the extended model are negative gives evidence that the width-averaged equilibria are stable in the extended model.

5.5 Two-dimensional variation of channel width.

How does the stability of the width-averaged equilibrium in the extended model change for a channel wider than 1 km? The accuracy and largest eigenvalue of this experiment are shown in figure 14.

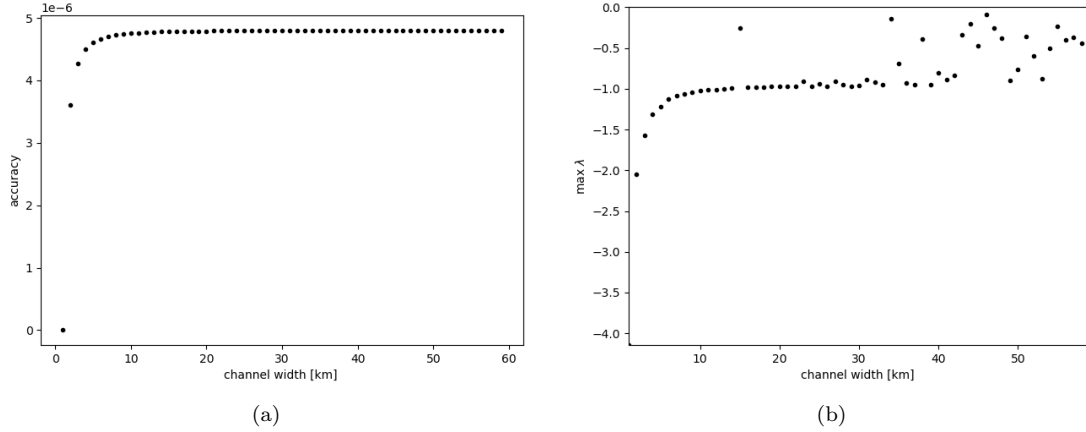


Figure 14: *The width-averaged equilibrium solutions in a width varied extended model. The width is varied between 1 km to 60 km.*

(a) *The accuracy in the extended model*

(b) *The largest eigenvalues in the extended model.*

In figure 14a it can be seen that the accuracy drops rapidly to $4.8 \cdot 10^{-6}$ at a channel width of 5 km and remains stable for wider channels. An accuracy of $4.8 \cdot 10^{-6}$ means that this solution is close to an equilibrium solution. The maximum eigenvalues seen in figure 14b increase from -4.1 to roughly -1 . However, after 30 km, no trend is visible. Again, the large number of discontinuities suggests that the method is not fully correct as the eigenvalues should be continuous. These results give evidence that for channels with a width of 30 km or less, the one-dimensional width averaged solution might be stable in the extended model. After 30 km, the eigenvalues show such discontinuous behaviour that no conclusions can be drawn anymore.

These results suggest that the width-averaged solutions could be stable in the expanded model even for wider channels. Physically, this is expected as the model has no forces that can create two-dimensional patterns. These patterns could arise if the model is expanded even further to take Coriolis effects into account. The Coriolis effects can only be neglected for narrow channels. However, since there are discontinuities in the eigenvalues, no real stability arguments can be provided. Further analysis is needed to prove the stability of the width-averaged solutions in the extended model.

6 Conclusion

In this thesis, the first steps are taken to extend the width-averaged morphodynamical model of Deng et al. (2020) to a two-dimensional model. To do this, a new extended model has been derived, the solutions agree with the solutions observed from the width-averaged model. The physical interpretation of the equilibrium solution provides the opportunity to capture the behaviour of the entire solution in three system-specific characteristics: minimal water depth, the lowest maximal water flow, and mean sediment transport. The changes of the equilibrium solutions under the variation of the phase, wave amplitude and inlet depth are analysed in terms of these characteristics. From these experiments, the complex behaviour known as limit point bifurcations arises for specific parameters. This strengthens the theory behind these limit point bifurcations formed by Deng et al. (2020). These bifurcations result in a parameter region where no solution can be found. Physically, this means that systems that are within such regions will eventually get clogged up by sediment. The width-averaged equilibrium solutions remain an accurate approximation in the two-dimensional expanded model. However, during the stability analysis, the observed eigenvalues give unexpected discontinuous behaviour, suggesting that the numerical Jacobian used has some unforeseen problems. These problems are not reflected in the equilibria found, as these solutions converge during calculation. Despite the discontinuities, the negative eigenvalues suggest that the width-averaged equilibria are stable in the expanded model. Further analysis of the stability under varying width suggests that the width-averaged equilibrium solution remains stable until a width of 30 km. However, for such large channels, the Coriolis effect should be taken into account.

Further research is required to prove that the width-averaged equilibria are truly stable in the two-dimensional morphodynamical models by improving the eigenvalue analysis done in this thesis. Additionally, the Coriolis effects can be included to calculate what systems can be approximated by the width-averaged model. Follow-up research might also use better optimized code and better equipment to speed up the process to be able to achieve higher resolution.

Bibliography

- Deng, X., Meerman, C., Boelens, T., de Mulder, T., Salles, P., & Schuttelaars, H. (2020). *Morphodynamic equilibria in double inlet system: Multiplicity and stability* [Manuscript submitted for publication.].
- de Swart, H., & Schuttelaars, H. (1997). An idealized long-term morphodynamic model of a tidal embayment.
- de Swart, H., & Zimmerman, J. (2009). Morphodynamics of tidal inlet systems. *Annual Review of Fluid Mechanics*, 41(1), 203–229. <https://doi.org/10.1146/annurev.fluid.010908.165159>
- Elias, E., van der Spek, A., Wang, Z., & de Ronde, J. (2012). Morphodynamic development and sediment budget of the dutch wadden sea over the last century. *Netherlands Journal of Geosciences - Geologie en Mijnbouw*, 91(3), 293–310. <https://doi.org/10.1017/S0016774600000457>
- Oppenheimer, M., Glavovic, B., & et al. (2019). Special report on the ocean and cryosphere in a changing climate. Intergovernmental Panel on Climate Change.
- Rozendaal, M. (2019). *An idealised morphodynamic model of a tidal inlet and the adjacent sea* [Master thesis].
- ter Brake, M., & Schuttelaars, H. (2010). Modeling equilibrium bed profiles of short tidal embayments. *Ocean Dynamics*, 60, 183–204. <https://doi.org/10.1007/s10236-009-0232-3>
- Vuik, C., & Lahaye, D. (2019). Scientific computing (wi4201). *Zoom earth*. (n.d.). <https://zoom.earth/> (accessed: 04.05.2021)

Appendix

The details needed to understand and create this thesis were not mentioned in the main text to keep it readable. These details are treated in the Appendix. First, a link to the repository with the used code is given. The next part of the Appendix is split up into three parts: Appendix A, contains the derivations of the shallow water equation used in chapter 2. Appendix B contains the derivations of the suspended sediment concentration equation used in chapter 2. Appendix C contains lengthy discretized boundary conditions and the reference to the code used in this thesis.

The code

During this thesis, a Python code was developed from scratch. The code can be found in a GitHub repository that is linked to the QR-code shown in figure 15. In this repository, the data of each experiment can be found as each equilibrium profile is saved as a unique data frame, the structured code to run the program, and the outdated code that was disregarded during the creation of the code. Additionally, The PowerPoint file used to create the figures is included in the repository. Feel free to use anything that can be found in the repository.

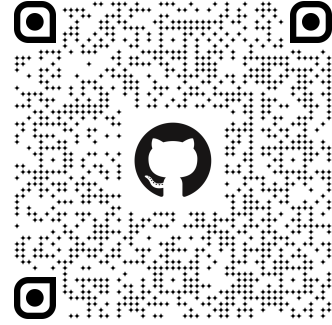


Figure 15: A QR-code to the repository of the newly developed python code.

URL:https://github.com/bverhage/BachelorThesis_moprhodynamical_equilibria_2D_double_inlet

The derivations

The following two Appendix chapters contain the derivation of the shallow water equations (Eqs. (2.1) and (2.2)) and the derivation of the suspended sediment concentration equation (Eq. (2.5)). The derivation of the bed evolution equation follows similar patterns however not treated in this Appendix.

A Derivation of depth-averaged shallow water equations

This derivation is heavily inspired by the derivations made in chapter 2 of the master thesis of Marco Rozendaal (2019). The main difference is the notation to be able to compactly denote the three-dimensional equations. For the full in-depth derivation see Rozendaal (2019).

The depth averaged shallow water equations (2.1) and (2.2) are derived from the original three-dimensional balances. This derivation consists of three parts. In the first part, the three-dimensional balances are stated and the Reynolds average is taken to prevent unwanted turbulent effects. In the second part (2.1) is derived. In the third part, (2.2) is derived.

A.1 Three-dimensional Reynolds averaged water equations

Consider a three-dimensional water channel as domain (see figure 16). Assume that water can only flow in and out of the channel through the front and back boundary. These boundaries physically correspond to the seaward boundaries, connected to the open sea.

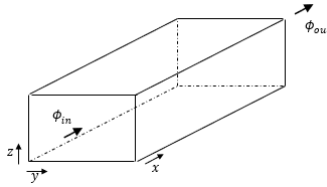


Figure 16: Domain under consideration. Φ_{in} and Φ_{out} denote the open boundaries. x is along the channel y denotes the correctional variables and z denotes the height.

For now, we only consider the behaviour of what happens in the interior of the domain. We do not yet consider the boundaries of this domain. Therefore, for simplicity, consider the domain to be a box. Let $\mathbf{u}(x, y, z, t) = [u, v, w]^T$ be the vector containing the water velocities in the x, y and z directions as a function of position and time. From the conservation of mass it follows that the flow must be continuous, thus

$$\nabla \cdot \mathbf{u} = 0. \quad (\text{A.1})$$

A box of water on earth is subject to a number of phenomena, being convection, Coriolis, pressure difference, viscous stress, and gravitational interactions. The effects of these phenomena are summarized in the Navier-Stokes equation

$$\frac{\partial}{\partial t} \mathbf{u} + \underbrace{[\mathbf{u} \cdot \nabla] \mathbf{u}}_{\text{conv.}} + \underbrace{\begin{bmatrix} 0 & -f & f^* \\ f & 0 & 0 \\ -f^* & 0 & 0 \end{bmatrix} \mathbf{u}}_{\text{cor.}} = \underbrace{-\frac{\nabla p}{\rho}}_{\text{press.}} + \underbrace{\nu \nabla^2 \mathbf{u}}_{\text{visc.}} + \underbrace{\begin{bmatrix} 0 \\ 0 \\ -g \end{bmatrix}}_{\text{grav.}}, \quad (\text{A.2})$$

here ρ denotes fluid density, p the pressure, ν the kinematic viscosity and g the gravitational acceleration. The Coriolis interaction is captured in the matrix stated in (A.2). For simplicity this matrix will be notated as $[\Omega]$. In this matrix, the elements $f = 2\Omega \sin(\phi)$ and $f^* = 2\Omega \cos(\phi)$ that are given by the Coriolis effect and the reciprocal Coriolis effect, here Ω angular velocity earth and ϕ the geographic latitude. The conservative form of (A.2) is

$$\mathbf{u}_t + \nabla \cdot [\mathbf{u} \otimes \mathbf{u}] + [\Omega] \mathbf{u} = -\frac{\nabla p}{\rho} + \nu \nabla^2 \mathbf{u} + \begin{bmatrix} 0 \\ 0 \\ -g \end{bmatrix}, \quad (\text{A.3})$$

here \otimes denotes the outer product, note that all conserved quantities are now behind a differential operator. Eq. (A.3) describes all conserved flows, both turbulent and laminar flows. To filter out the turbulent flow, a Reynolds decomposition average over time is used. The flow is decomposed into the mean and fluctuating parts

$$\mathbf{u} = \langle \mathbf{u} \rangle + \mathbf{u}', \quad (\text{A.4})$$

with the property that $\langle \mathbf{u}' \rangle = 0$. Let (A.3) be Reynolds averaged, then linearity gives

$$\langle \mathbf{u} \rangle_t + \nabla \cdot [\langle \mathbf{u} \rangle \otimes \langle \mathbf{u} \rangle + \langle \mathbf{u}' \otimes \mathbf{u}' \rangle] + [\Omega] \langle \mathbf{u} \rangle = -\frac{\nabla p}{\rho} + \nu \nabla^2 \langle \mathbf{u} \rangle + \begin{bmatrix} 0 \\ 0 \\ -g \end{bmatrix}. \quad (\text{A.5})$$

The unknown $\langle \mathbf{u}' \otimes \mathbf{u}' \rangle$ is known as Reynold stresses. These stresses are expressed in terms of viscosity

$$\langle \mathbf{u} \rangle_t + \nabla \cdot [\langle \mathbf{u} \rangle \otimes \langle \mathbf{u} \rangle] + [\Omega] \langle \mathbf{u} \rangle = -\frac{\nabla p}{\rho} + \nabla \cdot (\nu \nabla \langle \mathbf{u} \rangle - \langle \mathbf{u}' \otimes \mathbf{u}' \rangle) + \begin{bmatrix} 0 \\ 0 \\ -g \end{bmatrix}, \quad (\text{A.6})$$

here it is used that $\nabla^2 \equiv (\nabla \cdot \nabla)$. The Reynold stresses are approximated via the first-order closure. The horizontal eddies due to turbulence are assumed to be way larger than the vertical eddies, therefore the following approximation is done

$$\langle \mathbf{u}' \otimes \mathbf{u}' \rangle \approx -A_h \nabla_{xy} \langle \mathbf{u} \rangle - A_v \nabla_z \langle \mathbf{u} \rangle, \quad (\text{A.7})$$

where A_h and A_v are respectively, the horizontal and the vertical eddy viscosity coefficients and the differential is split up in the horizontal differential ∇_{xy} and vertical differential ∇_z are given by

$$\nabla = \begin{bmatrix} \frac{\partial}{\partial x} \\ \frac{\partial}{\partial y} \\ \frac{\partial}{\partial z} \end{bmatrix} = \begin{bmatrix} \frac{\partial}{\partial x} \\ \frac{\partial}{\partial y} \\ 0 \end{bmatrix} + \begin{bmatrix} 0 \\ 0 \\ \frac{\partial}{\partial z} \end{bmatrix} \equiv \nabla_{xy} + \nabla_z. \quad (\text{A.8})$$

The matrix that results from (A.7) is given by

$$\langle \mathbf{u}' \otimes \mathbf{u}' \rangle \approx - \begin{bmatrix} A_h \frac{\partial \langle u \rangle}{\partial x} & A_h \frac{\partial \langle u \rangle}{\partial y} & A_h \frac{\partial \langle u \rangle}{\partial z} \\ A_h \frac{\partial \langle v \rangle}{\partial x} & A_h \frac{\partial \langle v \rangle}{\partial y} & A_h \frac{\partial \langle v \rangle}{\partial z} \\ A_v \frac{\partial \langle w \rangle}{\partial x} & A_v \frac{\partial \langle w \rangle}{\partial y} & A_v \frac{\partial \langle w \rangle}{\partial z} \end{bmatrix}. \quad (\text{A.9})$$

Substituting (A.7) in (A.6), the following is obtained

$$\langle \mathbf{u} \rangle_t + \nabla \cdot [\langle \mathbf{u} \rangle \otimes \langle \mathbf{u} \rangle] + [\Omega] \langle \mathbf{u} \rangle = -\frac{\nabla p}{\rho} + \nabla \cdot ((\nu + A_h) \nabla_{xy} \langle \mathbf{u} \rangle + (\nu + A_v) \nabla_z \langle \mathbf{u} \rangle) + \begin{bmatrix} 0 \\ 0 \\ -g \end{bmatrix}. \quad (\text{A.10})$$

Eq. (A.10) is simplified by renaming $\mathbf{u} := \langle \mathbf{u} \rangle$ and calling $\mathcal{A}_h = \nu + A_h$ and $\mathcal{A}_v = \nu + A_v$ our new viscosity. Now we obtain the Reynolds Averaged Navier-Stokes equation

$$\mathbf{u}_t + [\mathbf{u} \cdot \nabla] \mathbf{u} + [\Omega] \mathbf{u} = -\frac{\nabla p}{\rho} + \nabla \cdot (\mathcal{A}_h \nabla_{xy} \mathbf{u} + \mathcal{A}_v \nabla_z \mathbf{u}) + \begin{bmatrix} 0 \\ 0 \\ -g \end{bmatrix}. \quad (\text{A.11})$$

Shallow water flow

Let L denote the characteristic horizontal scale and H the characteristic vertical scale. Similarly, let U and W denote the typical horizontal and vertical flow, respectively. An in-depth characteristic scale analysis of (A.1) done in Rozendaal (2019) reveals that the only feasible solution has $\frac{U}{L} \sim \frac{W}{H}$. Since in shallow water we have that $\frac{H}{L} \ll 1$ it follows that $W \ll U$. Consequently, the vertical flow w in (A.11) can be reduced to

$$\nabla_z p = -\rho g \hat{z}. \quad (\text{A.12})$$

A.2 Depth-averaged conservation of mass

The depth-averaged conservation of mass equation is obtained by integrating (A.1) and expressing the flow \mathbf{u} in the depth-averaged flow. The most important mathematical rule used during the derivation of the depth-averaged equations is the Leibniz's integration rule. It states that, if $L(\mathbf{u})$ is a linear operator applied on vector \mathbf{u} on a domain with variable boundaries $a(x, y)$ and $b(x, y)$ so that

$$\int_{a(x,y)}^{b(x,y)} L(\mathbf{u}) dz = L\left(\int_{a(x,y)}^{b(x,y)} \mathbf{u} dz\right) - [L(z)\mathbf{u}]_{a(x,y)}^{b(x,y)}. \quad (\text{A.13})$$

The depth averaged version of (A.1) is obtained by integrating from $h(x, y)$ to $H + \zeta(x, y)$. By linearity, the following expression

$$0 = \int_h^{H+\zeta} \nabla \cdot \mathbf{u} dz = \int_h^{H+\zeta} \nabla_{xy} \cdot \mathbf{u} dz + \int_h^{H+\zeta} \nabla_z \cdot \mathbf{u} dz. \quad (\text{A.14})$$

By the fundamental theorem of calculus, the last term is equal to $\hat{\mathbf{z}} \cdot \mathbf{u} \equiv w$. In the first term the Leibniz's integration rule is used with the linear operation $L(\mathbf{u}) = \nabla_{xy} \cdot \mathbf{u}$. It follows that

$$0 = \nabla_{xy} \cdot \left(\int_h^{H+\zeta} \mathbf{u} dz \right) - [\nabla_z \cdot \mathbf{u} - w]_h^{H+\zeta}. \quad (\text{A.15})$$

The depth-averaged water flow is defined as

$$\bar{\mathbf{u}} \equiv \frac{1}{H + \zeta - h} \int_h^{H+\zeta} \mathbf{u} dz. \quad (\text{A.16})$$

Substituting (A.16) in (A.15) gives

$$0 = \nabla_{xy} \cdot ((H + \zeta - h) \bar{\mathbf{u}}) + [h_x u + h_y v - w]_h - [\zeta_x u + \zeta_y v - w]_{H+\zeta}. \quad (\text{A.17})$$

In (A.17) the last two terms can be identified as the kinematic boundary conditions at the surface and bed of the domain. The kinematic boundary conditions follow from the free-surface boundary assuming that a fluid particle on the free surface always remains part of the free surface. For an in-depth derivation see Rozendaal (2019). The kinematic boundary conditions at the surface and bed are given by:

$$\begin{aligned} \zeta_t + \zeta_x u + \zeta_y v - w &= 0, \\ h_t + h_x u + h_y v - w &= 0. \end{aligned} \quad (\text{A.18})$$

Applying (A.18) to (A.17) gives us the depth-averaged conservation of mass equation as seen in (2.1) in Chapter 2,

$$0 = \nabla_{xy} \cdot ((H + \zeta - h) \bar{\mathbf{u}}) + \zeta_t - h_t. \quad (\text{A.19})$$

A.3 Depth-averaged conservation of momentum

The depth-averaged conservation of momentum is derived in two parts. First, the left and right hand sides of (A.11) are integrated. Then, both halves are added together to form the depth-averaged conservation of momentum in shallow water.

Left-hand side

Integrating the left hand side of (A.11) gives

$$\int_h^{H+\zeta} \mathbf{u}_t + \nabla \cdot [\mathbf{u} \otimes \mathbf{u}] + [\Omega] \mathbf{u} dz = \text{LHS}. \quad (\text{A.20})$$

Similarly to the derivation of the depth-averaged conservation of mass, the differential operator is split in a horizontal part ∇_{xy} and a vertical part ∇_z as seen in (A.8). Applying this to (A.20) gives

$$\int_h^{H+\zeta} \mathbf{u}_t dz + \int_h^{H+\zeta} (\nabla_{xy} + \nabla_z) \cdot [\mathbf{u} \otimes \mathbf{u}] dz + \int_h^{H+\zeta} [\Omega] \mathbf{u} dz = \text{LHS}. \quad (\text{A.21})$$

By linearity, the second integral can be written as two integrals. Note that the internal containing ∇_z is directly known by the fundamental theorem of calculus. For the integral containing ∇_{xy} and the one containing $\frac{\partial t}{\partial t}$ the Leibniz integration rules defined in Eq. (A.13) is used, where $L = \nabla_{xy}$ and $L = \frac{\partial}{\partial t}$ respectively. The depth-averaged water flow is defined in (A.16) on Eq. (A.21) can be recognized directly in the first and last term of Eq. (A.21). It follows that

$$\text{LHS} = [(H+\zeta-h)\bar{\mathbf{u}}]_t + \nabla_{xy} \cdot \left(\int_h^{H+\zeta} [\mathbf{u} \otimes \mathbf{u}] dz \right) - [\mathbf{u}(z_t + \mathbf{u} \cdot \nabla_{xy} z)]_h^{H+\zeta} + \hat{\mathbf{z}} \cdot [\mathbf{u} \otimes \mathbf{u}]_h^{H+\zeta} + (H+\zeta-h)[\Omega]\bar{\mathbf{u}}. \quad (\text{A.22})$$

Simplifying A.22 gives

$$\text{LHS} = [(H+\zeta-h)\bar{\mathbf{u}}]_t + \nabla_{xy} \cdot \left(\int_h^{H+\zeta} [\mathbf{u} \otimes \mathbf{u}] dz \right) + (H+\zeta-h)[\Omega]\bar{\mathbf{u}} - [\mathbf{u}(z_t + \mathbf{u} \cdot \nabla_{xy} z - w)]_h^{H+\zeta}, \quad (\text{A.23})$$

where the last term can be identified as the kinematic boundary conditions (see (A.18)). We analyse the second term a bit further. First, note that \mathbf{u} can be spit up in two parts: depth-averaged $\bar{\mathbf{u}}$, and the fluctuating part $\tilde{\mathbf{u}}$, such that $\mathbf{u} = \bar{\mathbf{u}} + \tilde{\mathbf{u}}$. Using this the the outer product of \mathbf{u} can be split up

$$[\mathbf{u} \otimes \mathbf{u}] = [(\bar{\mathbf{u}} + \tilde{\mathbf{u}}) \otimes (\bar{\mathbf{u}} + \tilde{\mathbf{u}})] = [\bar{\mathbf{u}} \otimes \bar{\mathbf{u}}] + 2[\tilde{\mathbf{u}} \otimes \bar{\mathbf{u}}] + [\tilde{\mathbf{u}} \otimes \tilde{\mathbf{u}}]. \quad (\text{A.24})$$

Now we need to integrate (A.24). Since $\tilde{\mathbf{u}}$ denotes the depth fluctuations and the depth averaged fluctuations must be zero it directly follows that $\int_h^{H+\zeta} \tilde{\mathbf{u}} dz = 0$. Consequently, the second term of (A.24) vanishes after integration. For the unknown third term, a similar closure problem arises and it is solved via an asymmetric parameterization

$$\int_h^{H+\zeta} [\tilde{\mathbf{u}} \otimes \tilde{\mathbf{u}}] dz = -\tilde{\mathcal{A}}_h (H + \zeta - h) \nabla \bar{\mathbf{u}}, \quad (\text{A.25})$$

where $\tilde{\mathcal{A}}_h$ denotes a new contribution to the viscosity terms. Thus, for the second term of (A.23) we get

$$\int_h^{H+\zeta} [\mathbf{u} \otimes \mathbf{u}] dz = (H + \zeta - h) \left([\bar{\mathbf{u}} \otimes \bar{\mathbf{u}}] - \tilde{\mathcal{A}}_h \nabla \bar{\mathbf{u}} \right). \quad (\text{A.26})$$

Substituting (A.26) in (A.23) gives

$$\text{LHS} = [(H + \zeta - h)\bar{\mathbf{u}}]_t + \nabla_{xy} \cdot \left((H + \zeta - h) \left\{ [\bar{\mathbf{u}} \otimes \bar{\mathbf{u}}] - \tilde{\mathcal{A}}_h \nabla \bar{\mathbf{u}} \right\} \right) + (H + \zeta - h)[\Omega]\bar{\mathbf{u}}. \quad (\text{A.27})$$

This can be simplified further by working out the product rule and identifying (A.19) to obtain the final expression for the LHS

$$\text{LHS} = (H + \zeta - h) (\bar{\mathbf{u}}_t + \nabla_{xy} \cdot [\bar{\mathbf{u}} \otimes \bar{\mathbf{u}}] - [\Omega]\bar{\mathbf{u}}) - \tilde{\mathcal{A}}_h \nabla_{xy} \cdot ((H + \zeta - h) \nabla \bar{\mathbf{u}}) \quad (\text{A.28})$$

Right hand side

The integrated right hand side equation of (A.11) becomes

$$\text{RHS} = \int_h^{H+\zeta} -\frac{\nabla p}{\rho} + \nabla \cdot (\mathcal{A}_h \nabla_{xy} \mathbf{u} + \mathcal{A}_v \nabla_z \mathbf{u}) + \begin{bmatrix} 0 \\ 0 \\ -g \end{bmatrix} dz. \quad (\text{A.29})$$

The most difficult term in (A.29) is the gradient of the pressure. The pressure in a water column at a certain height z is given by the atmospheric pressure plus the weight of the water above z . Thus

$$p = p_a + \rho g(H + \zeta - z), \quad (\text{A.30})$$

where p_a denotes the atmospheric pressure, ρ denotes the water density and g the gravitational acceleration. We first analyse the gradient of the pressure separately

$$\frac{-\nabla p}{\rho} = \frac{-1}{\rho} \nabla (p_a + \rho g(H + \zeta - z)) = -g \nabla (\zeta - z) = -g (\nabla_{xy} \zeta - \nabla_z z) = -g \nabla_{xy} \zeta + g \hat{\mathbf{z}}. \quad (\text{A.31})$$

When (A.31) is substituted in (A.29) it follows that the pressure term cancels the gravitational force. Thus (A.29) simplifies to

$$\text{RHS} = -g\nabla_{xy}\zeta \int_h^{H+\zeta} dz + \int_h^{H+\zeta} \nabla \cdot (\mathcal{A}_h \nabla_{xy} \mathbf{u} + \mathcal{A}_v \nabla_z \mathbf{u}) dz. \quad (\text{A.32})$$

Combining this together with the horizontal and vertical separation of $\nabla = \nabla_{xy} + \nabla_z$, then (A.32) changes to

$$\text{RHS} = -g(H + \zeta - h)\nabla_{xy}\zeta + \int_h^{H+\zeta} (\nabla_{xy} + \nabla_z) \cdot (\mathcal{A}_h \nabla_{xy} \mathbf{u} + \mathcal{A}_v \nabla_z \mathbf{u}) dz. \quad (\text{A.33})$$

Again, the integration of ∇_z is handled using the fundamental theorem of calculus to obtain $\hat{\mathbf{z}}$. Eq. (A.33) can be rewritten as

$$\text{RHS} = -g(H + \zeta - h)\nabla_{xy}\zeta + \mathcal{A}_h \int_h^{H+\zeta} \nabla_{xy} \cdot \nabla_{xy} \mathbf{u} dz + \mathcal{A}_v [\hat{\mathbf{z}} \cdot \nabla_z \mathbf{u}]_h^{H+\zeta}. \quad (\text{A.34})$$

In (A.34) the Leibniz integration rule is applied to the second term, which gives

$$\int_h^{H+\zeta} \nabla_{xy} \cdot \nabla_{xy} \mathbf{u} dz = \nabla_{xy} \cdot ((H + \zeta - h)\nabla_{xy} \bar{\mathbf{u}}) - [\nabla_{xy} \mathbf{u} \cdot \nabla_{xy} z]_h^{H+\zeta} H + \zeta. \quad (\text{A.35})$$

Substituting (A.35) in to the (A.34) gives

$$\text{RHS} = -g(H + \zeta - h)\nabla_{xy}\zeta + \mathcal{A}_h \nabla_{xy} \cdot ((H + \zeta - h)\nabla_{xy} \bar{\mathbf{u}}) - \mathcal{A}_h [\nabla_{xy} \mathbf{u} \cdot \nabla_{xy} z]_h^{H+\zeta} + \mathcal{A}_v [\hat{\mathbf{z}} \cdot \nabla_{xy} \mathbf{u}]_h^{H+\zeta}. \quad (\text{A.36})$$

Which can be simplified to

$$\text{RHS} = -g(H + \zeta - h)\nabla_{xy}\zeta + \mathcal{A}_h \nabla_{xy} \cdot ((H + \zeta - h)\nabla_{xy} \bar{\mathbf{u}}) - [\mathcal{A}_u \nabla_{xy} \mathbf{u} \cdot \nabla_{xy} z - \mathcal{A}_v \hat{\mathbf{z}} \cdot \nabla_{xy} \mathbf{u}]_h^{H+\zeta}. \quad (\text{A.37})$$

Note that in this expression the horizontal shear stress appears, which is given by

$$\frac{1}{\rho} \boldsymbol{\tau}_{\text{horizontal}} = \nu [\nabla_{xy} \mathbf{u}] \hat{\mathbf{n}}, \quad (\text{A.38})$$

here, ν the kinematic viscosity, can be replaced by the effective horizontal and vertical eddy viscosity coefficients \mathcal{A}_h and \mathcal{A}_v . The horizontal normal vector $\hat{\mathbf{n}} = [-\frac{\partial z}{\partial x}, -\frac{\partial z}{\partial y}, 1]^T = -\nabla_{xy} z + \hat{\mathbf{z}}$. Thus, it follows that (A.37) can be simplified even further to

$$\text{RHS} = -g(H + \zeta - h)\nabla_{xy}\zeta + \mathcal{A}_h \nabla_{xy} \cdot ((H + \zeta - h)\nabla_{xy} \bar{\mathbf{u}}) + \boldsymbol{\tau}_{\text{wind}} - \boldsymbol{\tau}_{\text{bed}}, \quad (\text{A.39})$$

here we assume that the shear stress induced by the wind is negligible and for the bed stress the Lorentz linearization is used. The Lorentz linearization states that $\boldsymbol{\tau}_{\text{bed}} = r^* \bar{\mathbf{u}}$ resulting in the final RHS equation

$$\text{RHS} = -g(H + \zeta - h)\nabla_{xy}\zeta + \mathcal{A}_h \nabla_{xy} \cdot ((H + \zeta - h)\nabla_{xy} \bar{\mathbf{u}}) - r^* \bar{\mathbf{u}}, \quad (\text{A.40})$$

here the drag coefficient $r^* \equiv \frac{8}{3\pi} C_d U$.

Total equation

Combining both the LHS of (A.28) and the RHS of (A.40) and dividing by the water depth $(H + \zeta - h)$ gives the total expression

$$\bar{\mathbf{u}}_t + \nabla_{xy} \cdot [\bar{\mathbf{u}} \otimes \bar{\mathbf{u}}] - [\Omega] \bar{\mathbf{u}} - \frac{\tilde{\mathcal{A}}_h \nabla_{xy} \cdot ((H + \zeta - h)\nabla_{xy} \bar{\mathbf{u}})}{H + \zeta - h} = -g\nabla_{xy}\zeta + \frac{\mathcal{A}_h \nabla_{xy} \cdot ((H + \zeta - h)\nabla_{xy} \bar{\mathbf{u}}) - r^* \bar{\mathbf{u}}}{H + \zeta - h}. \quad (\text{A.41})$$

Rearranging (A.41) and combining both viscosity constants $\hat{\mathcal{A}}_h \equiv \mathcal{A}_h + \tilde{\mathcal{A}}_h$ gives

$$\bar{\mathbf{u}}_t + \nabla_{xy} \cdot [\bar{\mathbf{u}} \otimes \bar{\mathbf{u}}] - [\Omega] \bar{\mathbf{u}} = -g\nabla_{xy}\zeta + \frac{\hat{\mathcal{A}}_h \nabla_{xy} \cdot ((H + \zeta - h)\nabla_{xy} \bar{\mathbf{u}}) - r^* \bar{\mathbf{u}}}{H + \zeta - h}. \quad (\text{A.42})$$

After scaling analysis it turns out that the contribution of the viscosity term is negligible, thus (A.43) can be approximated by

$$\overline{\mathbf{u}}_t + \nabla_{xy} \cdot [\overline{\mathbf{u}} \otimes \overline{\mathbf{u}}] - [\Omega] \overline{\mathbf{u}} = -g \nabla_{xy} \zeta + \frac{-r^* \overline{\mathbf{u}}}{H + \zeta - h}. \quad (\text{A.43})$$

This can be identified as the conservative form of conservation of momentum equation used in Chapter 2 Eq. (2.2).

B Derivation of suspended sediment concentration equation

This derivation is inspired by the derivation done in ter Brake and Schuttelaars (2010) in Appendix A: Derivation of the general 1D concentration equation. The three-dimensional suspended sediment concentration within the domain is defined as $C(x, y, z, t)$. By assumption, no suspended sediment can be created or destroyed in the interior of the domain, thus the continuity equation must be satisfied

$$C_t + \nabla \cdot (\mathbf{F}_a + \mathbf{F}_d + \mathbf{F}_s) = 0, \quad (\text{B.1})$$

here \mathbf{F}_a denotes the advective transport, \mathbf{F}_d diffusion and \mathbf{F}_s denotes the transport due to erosion and deposition. Advection transport in (B.1) is given by

$$\mathbf{F}_a = C \mathbf{u}, \quad (\text{B.2})$$

here \mathbf{u} denotes the three-dimensional water velocity. The diffusive transport is split up in two horizontal and vertical diffusive transport with $\nabla = \nabla_{xy} + \nabla_z$. The suspended sediment diffusive transport is given by

$$\mathbf{F}_d = -K_h \nabla_{xy} C - K_v \nabla_z C. \quad (\text{B.3})$$

The transport due to sedimentation in (B.1) is given by

$$\mathbf{F}_s = -C \omega_s \hat{\mathbf{z}}, \quad (\text{B.4})$$

here ω_s denotes the settling velocity. Applying (B.2), (B.3) and (B.4) on (B.1) gives the total transport

$$C_t + \nabla \cdot (C(\mathbf{u} - \omega_s \hat{\mathbf{z}})) - \nabla \cdot (K_h \nabla_{xy} C + K_v \nabla_z C) = 0. \quad (\text{B.5})$$

For (B.5) the only morphodynamically active boundary is the bed and thus the boundary transport property is given by

$$-(\mathbf{F}_s + \mathbf{F}_d) \cdot \hat{\mathbf{n}}_{\text{bed}} = S_*, \quad (\text{B.6})$$

where $\hat{\mathbf{n}}_{\text{bed}} = -\nabla_{xy} h + \hat{\mathbf{z}}$ is the normal pointing out of the bed, and S_* the total sedimentation flux. The total sedimentation flux exists of the erosion flux E and the deposition flux D such that $S_* = E - D$, where

$$E = \omega_s c_a, \text{ and } D = \omega_s c_b. \quad (\text{B.7})$$

Here, c_a is the reference concentration and has to be parametrized in terms of the flow conditions, while c_b is the concentration near the bottom and follows from the solution of the concentration equation. See ter Brake and Schuttelaars (2010) for more information.

Depth integration

To be able to express the three-dimensional continuity equation (B.1) in depth integrated variables. Equation (B.1) is integrated over the a vertical column to obtain

$$0 = \int_h^{H+\zeta} C_t dz + \int_h^{H+\zeta} \nabla_{xy} \cdot \mathbf{F} dz + \int_h^{H+\zeta} \nabla_z \cdot \mathbf{F} dz. \quad (\text{B.8})$$

Applying the Leibniz integration rule (see (A.13)) on (B.8) gives

$$0 = \left(\int_h^{H+\zeta} C dz \right)_t + \nabla_{xy} \cdot \left(\int_h^{H+\zeta} \mathbf{F} dz \right) - [C \frac{\partial z}{\partial t} + \nabla_{xy} z \cdot \mathbf{F} - \hat{\mathbf{z}} \cdot \mathbf{F}]_h^{H+\zeta}, \quad (\text{B.9})$$

where the total transport can be split up $\mathbf{F} = \mathbf{F}_a + \mathbf{F}_d + \mathbf{F}_s$. The last term of (B.9) can be identified as the normal vector $\hat{\mathbf{n}}$, pointing out of the top or bottom boundaries. Substituting this in (B.9) gives

$$0 = \left(\int_h^{H+\zeta} C dz \right)_t + \nabla_{xy} \cdot \left(\int_h^{H+\zeta} \mathbf{F} dz \right) - [C \frac{\partial z}{\partial t} + \hat{\mathbf{n}} \cdot \mathbf{F}_a + \hat{\mathbf{n}} \cdot (\mathbf{F}_s + \mathbf{F}_d)]_h^{H+\zeta}. \quad (\text{B.10})$$

Analysis of the last term of (B.10) gives

$$\begin{aligned} & -[C \frac{\partial \zeta}{\partial t} + \hat{\mathbf{n}} \cdot \mathbf{F}_a + \hat{\mathbf{n}} \cdot (\mathbf{F}_s + \mathbf{F}_d)]_{H+\zeta} + [C \frac{\partial h}{\partial t} + \hat{\mathbf{n}} \cdot \mathbf{F}_a + \hat{\mathbf{n}} \cdot (\mathbf{F}_s + \mathbf{F}_d)]_h \\ & = -[C \frac{\partial \zeta}{\partial t} + \hat{\mathbf{n}} \cdot (C\mathbf{u}) + 0]_{H+\zeta} + [C \frac{\partial h}{\partial t} + \hat{\mathbf{n}} \cdot (C\mathbf{u}) - S_*]_h, \end{aligned} \quad (\text{B.11})$$

where the last term can be identified as the kinematic boundary condition (see (A.18)) with which it follows that (B.11) can be written as

$$= -[C(\frac{\partial \zeta}{\partial t} + \zeta_x u + \zeta_y v - w)]_{H+\zeta} + [C(\frac{\partial h}{\partial t} + h_x u + h_y v - w) - S_*]_h = -[S_*]_h. \quad (\text{B.12})$$

Thus, the last term of (B.9) becomes S_* . Now we want to express (B.9) in terms of the depth-integrated concentration. The depth-integrated concentration \mathcal{C} is defined as

$$\mathcal{C} \equiv \int_h^{H+\zeta} C \, dz = \frac{1}{H+\zeta-h} \bar{C}, \quad (\text{B.13})$$

here \bar{C} is the depth-averaged suspended sediment concentration. Substituting (B.13) and the definition of \mathbf{F} in (B.10) gives

$$0 = \mathcal{C}_t + \nabla_{xy} \cdot \left(\int_h^{H+\zeta} C(\mathbf{u} - w_s \hat{\mathbf{z}}) - K_h \nabla_{xy} C - K_v \nabla_z C \, dz \right) - S_*. \quad (\text{B.14})$$

Note that $\nabla_{xy} \cdot \hat{\mathbf{z}} = 0$ thus the sedimentation transport in (B.14) can be neglected. Additionally $\nabla_{xy} \cdot \nabla_{xy} C = 0$, applying this to (B.14) gives

$$0 = \mathcal{C}_t + \nabla_{xy} \cdot \left(\int_h^{H+\zeta} C\mathbf{u} \, dz \right) - K_h \nabla_{xy} \cdot \left(\int_h^{H+\zeta} \nabla_{xy} C \, dz \right) - S_*. \quad (\text{B.15})$$

The concentration can be split up in the depth-averaged part and the perturbed part; $C = \bar{C} + C'$. Similarly the flow can be described by $\mathbf{u} = \bar{\mathbf{u}} + \mathbf{u}'$. This is used to calculate the second term of (B.15) as follows

$$\int_h^{H+\zeta} C\mathbf{u} \, dz = \int_h^{H+\zeta} (\bar{C} + C')(\bar{\mathbf{u}} + \mathbf{u}') \, dz, \quad (\text{B.16})$$

this is simplified by working out the multiplications and using that \bar{C} and $\bar{\mathbf{u}}$ are not dependent on z , and the average of the perturbed variables is zero, it follows that

$$\int_h^{H+\zeta} \bar{C}\bar{\mathbf{u}} \, dz + \int_h^{H+\zeta} \bar{C}\mathbf{u}' \, dz + \int_h^{H+\zeta} C'\bar{\mathbf{u}} \, dz + \int_h^{H+\zeta} C'\mathbf{u}' \, dz = \bar{C}\bar{\mathbf{u}}(H+\zeta-h) + 0 + 0 + \int_h^{H+\zeta} C'\mathbf{u}' \, dz. \quad (\text{B.17})$$

The difficult term in (B.17) is the last term. This term can be approximated as $C'\mathbf{u}' = -K_b \nabla_{xy} C$ as stated in ter Brake and Schuttelaars (2010). With this approximation, we can go back to the original problem (B.15), giving

$$\mathcal{C}_t + \nabla_{xy} \cdot (\bar{C}\bar{\mathbf{u}}(H+\zeta-h)) - (K_h + K_b) \nabla_{xy} \cdot \left(\int_h^{H+\zeta} \nabla_{xy} C \, dz \right) - S_* = 0. \quad (\text{B.18})$$

In the second term in (B.18) the depth averaged concentration can be changed to the depth integrated concentration \mathcal{C} via (B.13). The diffusivity constants are combined to $\tilde{K} = K_h + K_b$. The Leibniz integration rule is applied to the third term of (B.18) to obtain

$$\mathcal{C}_t + \nabla_{xy} \cdot (\mathcal{C}\bar{\mathbf{u}}) - \tilde{K} \nabla_{xy} \cdot \left(\nabla_{xy} \mathcal{C} - [C \nabla_{xy} z]_h^{H+\zeta} \right) = S_*. \quad (\text{B.19})$$

We now use that we assume the concentration at the top and bottom to be known and equal to $C|_h = c_b$ and $C|_z = c_b \exp \frac{-\omega_s}{K_v}(z-h)$ respectively, for more information see ter Brake and Schuttelaars (2010) page 201. $C|_z$ can be expressed in terms of \mathcal{C} by integrating

$$\mathcal{C} = c_b \frac{K_v}{\omega_s} (1 - e^{\frac{-\omega_s}{K_v}(H+\zeta-h)}). \quad (\text{B.20})$$

Rearranging (B.20) gives an expression for $c_b = C|_h$

$$c_b = \frac{\omega_s}{K_v} \mathcal{C} \frac{1}{1 - e^{-\frac{\omega_s}{K_v}(H+\zeta-h)}} \equiv \frac{\omega_s}{K_v} \mathcal{C} \beta_b. \quad (\text{B.21})$$

With this, the part $[C\nabla_{xy}z]_h^{H+\zeta}$ in (B.19) is written as

$$[C\nabla_{xy}z]_h^{H+\zeta} = c_b e^{-\frac{\omega_s}{K_v}(H+\zeta-h)} \nabla_{xy}\zeta - c_b \nabla_{xy}h = \frac{\omega_s}{K_v} \mathcal{C} (\beta_t \nabla_{xy}\zeta - \beta_b \nabla_{xy}h). \quad (\text{B.22})$$

Applying this to (B.19) gives

$$\mathcal{C}_t + \nabla_{xy} \cdot (\mathcal{C}\bar{\mathbf{u}}) - \tilde{K} \nabla_{xy} \cdot \left(\nabla_{xy} \mathcal{C} - \frac{\omega_s}{K_v} (\beta_t \nabla_{xy}\zeta - \beta_b \nabla_{xy}h) \mathcal{C} \right) = S_*. \quad (\text{B.23})$$

Eq. (B.23) is almost the desired form and the only part left is the erosion deposition term. From ter Brake and Schuttelaars (2010) it follows that we can write the erosion as $E = \alpha \bar{\mathbf{u}} \cdot \bar{\mathbf{u}}$, with $\alpha = \rho_s(1-p) \frac{\Gamma \omega_s}{u_*^2 C} c_d$. Together with (B.7) this means that the total sedimentation flux $S_* = E - D$ becomes

$$S_* = \alpha \bar{\mathbf{u}} \cdot \bar{\mathbf{u}} - \frac{\omega_s^2 \beta_b}{K_v} \mathcal{C}. \quad (\text{B.24})$$

Combining (B.24) with (B.23) gives the final depth integrated suspended sediment equation

$$\mathcal{C}_t + \nabla_{xy} \cdot (\mathcal{C}\bar{\mathbf{u}}) - \tilde{K} \nabla_{xy} \cdot \left(\nabla_{xy} \mathcal{C} - \frac{\omega_s}{K_v} (\beta_t \nabla_{xy}\zeta - \beta_b \nabla_{xy}h) \mathcal{C} \right) = \alpha \bar{\mathbf{u}}^2 - \frac{\omega_s^2}{K_v} \beta_b \mathcal{C}, \quad (\text{B.25})$$

Which is used in chapter 2, equation (2.5).

C The boundary conditions of the discretization

The boundary conditions of discretized $\mathbf{f}(\mathbf{x})$ denoted in Eq. (4.1) is given by

$$\begin{aligned}
\mathbf{f}_{\zeta^s} &= -\zeta^s + 0, & i = 1, & j \in \{1, \dots, N_y + 1\}, \\
\mathbf{f}_{\zeta^s} &= -\zeta^s + A_{r, \sin(\phi)} & i = N_x + 1, & j \in \{1, \dots, N_y + 1\}, \\
\mathbf{f}_{\zeta^s} &= -\zeta^s - (1 - \mathbf{h}) \circ ([L_x] \mathbf{u}^c + [L_y]_f \mathbf{v}^c) \\
&\quad + \mathbf{u}^c \circ [L_x] \mathbf{h} + \mathbf{v}^c \circ [L_y]_f \mathbf{h}, & i \in \{1, \dots, N_x + 1\}, & j = 1, \\
\mathbf{f}_{\zeta^s} &= -\zeta^s - (1 - \mathbf{h}) \circ ([L_x] \mathbf{u}^c + [L_y]_b \mathbf{v}^c) \\
&\quad + \mathbf{u}^c \circ [L_x] \mathbf{h} + \mathbf{v}^c \circ [L_y]_b \mathbf{h}, & i \in \{1, \dots, N_x + 1\}, & j = N_y + 1, \\
\mathbf{f}_{\zeta^c} &= -\zeta^c + 1, & i = 1, & j \in \{1, \dots, N_y + 1\}, \\
\mathbf{f}_{\zeta^c} &= -\zeta^c + A_{r, \cos(\phi)} & i = N_x + 1, & j \in \{1, \dots, N_y + 1\}, \\
\mathbf{f}_{\zeta^c} &= -\zeta^c + (1 - \mathbf{h}) \circ ([L_x] \mathbf{u}^s + [L_y]_f \mathbf{v}^s) \\
&\quad - \mathbf{u}^s \circ [L_x] \mathbf{h} - \mathbf{v}^s \circ [L_y]_f \mathbf{h}, & i \in \{1, \dots, N_x + 1\}, & j = 1, \\
\mathbf{f}_{\zeta^c} &= -\zeta^c + (1 - \mathbf{h}) \circ ([L_x] \mathbf{u}^s + [L_y]_b \mathbf{v}^s) \\
&\quad - \mathbf{u}^s \circ [L_x] \mathbf{h} - \mathbf{v}^s \circ [L_y]_b \mathbf{h}, & i \in \{1, \dots, N_x + 1\}, & j = N_y + 1, \\
\mathbf{f}_{u^s} &= -\mathbf{u}^s - \frac{r}{1 - \mathbf{h}} \circ \mathbf{u}^c + \lambda_L^2 [L_x]_f \zeta^s, & i = 1, & j \in \{1, \dots, N_y + 1\}, \\
\mathbf{f}_{u^s} &= -\mathbf{u}^s - \frac{r}{1 - \mathbf{h}} \circ \mathbf{u}^c + \lambda_L^2 [L_x]_b \zeta^s, & i = N_x + 1, & j \in \{1, \dots, N_y + 1\}, \\
\mathbf{f}_{u^s} &= -\mathbf{u}^s - \frac{r}{1 - \mathbf{h}} \circ \mathbf{u}^c + \lambda_L^2 [L_x] \zeta^s, & i \in \{1, \dots, N_x + 1\}, & j = 1, \\
\mathbf{f}_{u^s} &= -\mathbf{u}^s - \frac{r}{1 - \mathbf{h}} \circ \mathbf{u}^c + \lambda_L^2 [L_x] \zeta^s, & i \in \{1, \dots, N_x + 1\}, & j = N_y + 1, \\
\mathbf{f}_{u^c} &= -\mathbf{u}^c + \frac{r}{1 - \mathbf{h}} \circ \mathbf{u}^s - \lambda_L^2 [L_x]_f \zeta^c, & i = 1, & j \in \{1, \dots, N_y + 1\}, \\
\mathbf{f}_{u^c} &= -\mathbf{u}^c + \frac{r}{1 - \mathbf{h}} \circ \mathbf{u}^s - \lambda_L^2 [L_x]_b \zeta^c, & i = N_x + 1, & j \in \{1, \dots, N_y + 1\}, \\
\mathbf{f}_{u^c} &= -\mathbf{u}^c + \frac{r}{1 - \mathbf{h}} \circ \mathbf{u}^s - \lambda_L^2 [L_x] \zeta^c, & i \in \{1, \dots, N_x + 1\}, & j = 1, \\
\mathbf{f}_{u^c} &= -\mathbf{u}^c + \frac{r}{1 - \mathbf{h}} \circ \mathbf{u}^s - \lambda_L^2 [L_x] \zeta^c, & i \in \{1, \dots, N_x + 1\}, & j = N_y + 1, \\
\mathbf{f}_{v^s} &= -\mathbf{v}^s - \frac{r}{1 - \mathbf{h}} \circ \mathbf{v}^c - \lambda_L^2 [L_y] \zeta^s, & i = 1, & j \in \{1, \dots, N_y + 1\}, \\
\mathbf{f}_{v^s} &= -\mathbf{v}^s - \frac{r}{1 - \mathbf{h}} \circ \mathbf{v}^c - \lambda_L^2 [L_y] \zeta^s, & i = N_x + 1, & j \in \{1, \dots, N_y + 1\}, \\
\mathbf{f}_{v^s} &= -\mathbf{v}^s - \frac{r}{1 - \mathbf{h}} \circ \mathbf{v}^c - \lambda_L^2 [L_y]_f \zeta^s, & i \in \{1, \dots, N_x + 1\}, & j = 1, \\
\mathbf{f}_{v^s} &= -\mathbf{v}^s - \frac{r}{1 - \mathbf{h}} \circ \mathbf{v}^c - \lambda_L^2 [L_y]_b \zeta^s, & i \in \{1, \dots, N_x + 1\}, & j = N_y + 1, \\
\mathbf{f}_{v^c} &= -\mathbf{v}^c + \frac{r}{1 - \mathbf{h}} \circ \mathbf{v}^s + \lambda_L^2 [L_y] \zeta^c, & i = 1, & j \in \{1, \dots, N_y + 1\}, \\
\mathbf{f}_{v^c} &= -\mathbf{v}^c + \frac{r}{1 - \mathbf{h}} \circ \mathbf{v}^s + \lambda_L^2 [L_y] \zeta^c, & i = N_x + 1, & j \in \{1, \dots, N_y + 1\}, \\
\mathbf{f}_{v^c} &= -\mathbf{v}^c + \frac{r}{1 - \mathbf{h}} \circ \mathbf{v}^s + \lambda_L^2 [L_y]_f \zeta^c, & i \in \{1, \dots, N_x + 1\}, & j = 1, \\
\mathbf{f}_{v^c} &= -\mathbf{v}^c + \frac{r}{1 - \mathbf{h}} \circ \mathbf{v}^s + \lambda_L^2 [L_y]_b \zeta^c, & i \in \{1, \dots, N_x + 1\}, & j = N_y + 1,
\end{aligned} \tag{C.1}$$

Where $[L_y]_f$ and $[L_y]_b$ denote the forward and backwards numerical finite difference matrices. The discretized boundary conditions for \mathbf{f}_C denoted in Eq. (4.6) read

$$\begin{aligned}
\mathbf{f}_C &= +\frac{1}{2}(\mathbf{u}^s \circ \mathbf{u}^s + \mathbf{u}^c \circ \mathbf{u}^c + \mathbf{v}^s \circ \mathbf{v}^s + \mathbf{v}^c \circ \mathbf{v}^c) - \beta \circ \mathcal{C}, & i = 1, \quad j \in \{1, \dots, N_y + 1\}, \\
\mathbf{f}_C &= +\frac{1}{2}(\mathbf{u}^s \circ \mathbf{u}^s + \mathbf{u}^c \circ \mathbf{u}^c + \mathbf{v}^s \circ \mathbf{v}^s + \mathbf{v}^c \circ \mathbf{v}^c) - \beta \circ \mathcal{C}, & i = N_x + 1, \quad j \in \{1, \dots, N_y + 1\}, \\
\mathbf{f}_C &= +\frac{1}{2}(\mathbf{u}^s \circ \mathbf{u}^s + \mathbf{u}^c \circ \mathbf{u}^c) - \beta \circ \mathcal{C}, & i \in \{1, \dots, N_x + 1\}, \quad j = 1, \\
\mathbf{f}_C &= +\frac{1}{2}(\mathbf{u}^s \circ \mathbf{u}^s + \mathbf{u}^c \circ \mathbf{u}^c) - \beta \circ \mathcal{C}, & i \in \{1, \dots, N_x + 1\}, \quad j = N_y + 1.
\end{aligned} \tag{C.2}$$

The discretized boundary conditions for \mathbf{f}_h denoted in Eq. (4.7) read

$$\begin{aligned}
\mathbf{f}_h &= -\mathbf{h} + 0, & i = 1, \quad j \in \{1, \dots, N_y + 1\}, \\
\mathbf{f}_h &= -\mathbf{h} + 1 - \frac{H^{II}}{H^I}, & i = N_x + 1, \quad j \in \{1, \dots, N_y + 1\}, \\
\mathbf{f}_h &= [L_y]_f \mathbf{h}, & i \in \{1, \dots, N_x + 1\}, \quad j = 1, \\
\mathbf{f}_h &= [L_y]_b \mathbf{h}, & i \in \{1, \dots, N_x + 1\}, \quad j = N_y + 1.
\end{aligned} \tag{C.3}$$